Icarus 328 (2019) 104–126

Contents lists available at ScienceDirect

Icarus

journal homepage: www.elsevier.com/locate/icarus

A comparison of multiple Rosetta data sets and 3D model calculations of 67P/Churyumov-Gerasimenko coma around equinox (May 2015)

R. Marschall[a,b,*], L. Rezac[c], D. Kappel[d], C.C. Su[e], S.-B. Gerig[b], M. Rubin[b], O. Pinzón-Rodríguez[b], D. Marshall[c], Y. Liao[f], C. Herny[b], G. Arnold[d], C. Christou[h], S.K. Dadzie[h], O. Groussin[g], P. Hartogh[c], L. Jorda[g], E. Kührt[d], S. Mottola[d], O. Mousis[g], F. Preusker[d], F. Scholten[d], P. Theologou[b], J.-S. Wu[e], K. Altwegg[b], R. Rodrigo[a], N. Thomas[b]

[a] International Space Science Institute, Hallerstrasse 6, Bern CH-3012, Switzerland
[b] Physikalisches Institut, University of Bern, Sidlerstr. 5, Bern CH-3012, Switzerland
[c] Max-Planck-Institut für Sonnensystemforschung, Justus-von-Liebig-Weg, 3, 37077 Göttingen, Germany
[d] Deutsches Zentrum für Luft- und Raumfahrt (DLR), Institut für Planetenforschung, Rutherfordstrasse 2, Berlin 12489, Germany
[e] Department of Mechanical Engineering, National Chiao Tung University, 1001 Ta-Hsueh Road, Hsinchu 30010, Taiwan
[f] Macau University of Science and Technology, Macau
[g] Laboratoire d'Astrophysique de Marseille, 38 Rue de Frederic Joliot-Curie, 13388 Marseille Cedex 13, France
[h] School of Engineering and Physical Sciences, Heriot-Watt University, Edinburgh EH14 4AS, Scotland, UK

ARTICLE INFO

Keywords:
Comets
67P/Churyumov-Gerasimenko
Coma
Dust
Dynamics

ABSTRACT

We have used the latest available shape model for gas and dust simulations of the inner coma of comet 67P/Churyumov-Gerasimenko for the period around May 2015 (equinox). We compare results from a purely insolation-driven model with a complementary set of observations made by ROSINA, VIRTIS, MIRO, and OSIRIS within the same period. The observations include - for the first time - inverted MIRO measurements of gas density, temperature and bulk velocity to constrain the model. The comparisons show that, as in November 2014 (Marschall et al., 2016), insolation-driven activity does not provide an adequate fit to the data. Both VIRTIS and MIRO observations indicate that emissions from the Hatmehit and Imhotep regions of the nucleus are strongly depleted in total gas, H_2O, and dust emissions in this case. The MIRO inversion provides a challenging constraint to the models as a consequence of the terminator orbit and nucleus pointing of the spacecraft. Nonetheless a consistent picture with a dominance of outgassing from the Hapi region, even at equinox, is clearly evident. An inhomogeneous model consistent with models proposed for the November 2014 time-frame was constructed and provides a better fit to the data. As far as we are aware this is the first time comae data from four Rosetta instruments have been used to constrain within one self-contained model the emission distribution at the nucleus surface and study the dynamics of the gas and dust outflow.

1. Introduction

As comets enter the inner solar system and get close enough to the Sun their volatile components start sublimating and drag with them dust particles resulting in spectacular dust tails that are commonly known. The determination of the activity distribution on the surface of a comet is a key goal of any mission to investigate a cometary nucleus. The Rosetta mission to comet 67P/Churyumov-Gerasimenko (hereafter 67P) included as one of five prime goals in the original Rosetta announcement of opportunity (RO-EST-AO-0001, 1st March 1995) "The development of cometary activity and the processes in the surface layer of the nucleus and in the inner coma". While some highly localized sources of dust have been identified on the nucleus of 67P (e.g. Fornasier et al., 2017), there remains a great uncertainty regarding the physical processes that are involved. There are several reasons for this: First, for imaging experiments (in visible wavelengths) the dust is used as a proxy for gas activity since the gas molecules have no optical emissions. Although there is a limited range of application to this approach, it breaks down when viewing the dust against a background of the illuminated nucleus. In all but a very few number of cases, the optical depth of the dust is far less than unity and hence it cannot be seen against the bright surface because the brightness of dust is

* Corresponding author.
E-mail addresses: raphael.marschall@issibern.ch, marschall@cosmoculus.net (R. Marschall).

https://doi.org/10.1016/j.icarus.2019.02.008
Received 28 August 2018; Received in revised form 23 January 2019; Accepted 11 February 2019
Available online 07 March 2019

contaminated by the scattered light of the nucleus. Second, the resolutions of the remote sensing instruments sensitive to molecule emissions (i.e. infrared and sub-mm spectrometers) are limited both spatially and temporally, such that common volume observations (such that the same coma region is fully in each instrument's field-of-view, FOV, at the same time) are not easy to reconstruct. Furthermore, all these observations rely on interpreting a line-of-sight (LOS) radiance propagating through a gas coma structure that is not homogeneous (in density, temperature, and velocity). In addition, often the optical depth of the medium in a given wavelength range is large such that it significantly complicates the analysis. Third, the densities measured at the spacecraft through particle sensors are obviously only local measurements. The frequent use of terminator orbits by the Rosetta spacecraft is another significant complication in their interpretation because local densities are measured at remote points remote from the main direction of outflow, namely in the sun-ward direction. Moreover the gas expansion from surface sources into the coma reduces the "contrast" between active and inactive regions when measurements are made from tens of kilometres above the surface leading to considerable ambiguity in such conclusions.

The aim of this work is to study the diverse data sets of Rosetta (including OSIRIS, VIRTIS, MIRO, ROSINA, and GIADA), constraining the gas emission into the coma and to establish whether the data are sufficient to reach appropriate conclusions on the activity distribution on the nucleus. Some work has already been published towards this end as will be discussed in detail in the following sections. We refer however to papers by Bieler et al. (2015), Fougere et al. (2016), Tenishev et al. (2016) and Marschall et al. (2016, hereafter M2016) as examples of the general approach being taken. However, there remains a considerable amount of work to be done to incorporate all the constraints. We focus here on the time around May 2015 (inbound equinox). For this period the activity was already significantly higher than for our previously studied periods of September–November 2014. While this period is a few months prior to perihelion, the spacecraft was close to the comet - in contrast to the period around perihelion - allowing high-resolution remote sensing observations and near-nucleus in-situ measurements that proved to be easier to connect. Moreover VIRTIS-M-IR data are only available until May 2015.

We will first discuss the gas and dust models involved in this work in Section 2 where we will also describe how the models relate to and can be compared to the different Rosetta instruments. In Section 3 we describe the different instruments we have focused on and the observations that were analysed. We then continue in Section 4 to describe the comparisons between the model and the data of the different instruments and what we can learn from them. Finally in Section 5 we summarize our conclusions coming from the different instruments.

2. DSMC model and coma calculations

The approach that we take was outlined by Marschall et al. (2016). We have built a series of models which allow us to compare at various stages model output with observables from several experiments on Rosetta. The chain is shown in Fig. 1 (after Marschall et al., 2017, hereafter M2017). The results from the DSMC gas dynamics program are compared with measurements from ROSINA/COPS, MIRO, and VIRTIS instruments. The results of the dust brightness calculations are compared to OSIRIS images. Below we introduce the different models involved and describe them in more detail in particular the assumptions taken. How the different instruments inform the input parameters will be discussed in Section 3.

2.1. DSMC package

The gas flow-field herein will be calculated using the Direct Simulation Monte Carlo (DSMC) technique. The code used is called UltraSPARTS[1] and is a commercialized derivative of the PDSC++ code (Su, 2013) used in previous papers (e.g. Marschall et al., 2017, 2016). PDSC++ is a C++ based, parallel DSMC code which is capable of simulating 2D, 2D-axisymmetric, and 3D flow fields. The code has been developed over the past 15 years (Wu and Lian, 2003; Wu et al., 2004; Wu and Tseng, 2005) and contains several important features including the implementation of 2D and 3D hybrid unstructured grids, a transient adaptive sub-cell method (TAS) for denser flows, and a variable time-step scheme (VTS). In the parallel version, computational tasks are distributed using the Message Passing Interface (MPI) protocol. A Domain Re-Decomposition (DRD) method, to optimize the parallel performance, has also been implemented (Liao, 2017). The improved UltraSPARTS (Ultra-fast Statistical PARTicle Simulation Package) has been applied first to 67P by Gerig et al. (2018).

2.2. Shape and coma grid model

The shape of the nucleus is vastly different from that expected prior to rendezvous (Lamy et al., 2006; Sierks et al., 2015), and the double-lobed structure about a "neck" has provoked much speculation about its origin (Davidsson et al., 2016; Jutzi and Benz, 2017). For activity studies, it has also provided significant challenges. The key aspect is that interaction of gas emitted from adjacent regions is enhanced in the region of the neck situated between the two lobes. The nucleus shape model (SHAP7) (Preusker et al., 2017) is shown in Fig. 2 with the morphological region definition (El-Maarry et al., 2016; Thomas et al., 2018). The 3D shape model of the nucleus was integrated into the simulation code with the help of a grid generation program, GRIDGEN program from Pointwise. The full resolution of the nucleus shape model - with about 44 million facets and a horizontal sampling of ~ 1 m and a vertical accuracy on the decimetre scale - cannot be used. The total number of grid elements must be restricted so that the gas dynamics computation can be run at all because of computational load and memory issues. Consequently, the final model passed to the gas dynamics simulation has been decimated to around 400,000 surface facets. Care needs to be taken with the surface definition as significant artificial smoothing of the surface can result. Our current grid deviates from the high-resolution shape model at the surface with an RMS error of ~30 cm in elevation. The computational domain extends out to 10 km from the nucleus centre of mass in the nominal case. This is usually sufficient except in high gas density cases. An example of the inner section of an unstructured grid is shown in Fig. 3. The simulation domain used in this work consist of over 13 million tetrahedron cells.

2.3. Thermal modelling of the nucleus and the gas emission rates

In order to initiate the gas dynamics simulation, a surface boundary condition is required. This boundary condition must specify the gas production rate at each surface facet and the initial gas temperature. Further complexity can arise if the velocity distribution function at the surface is not a half-Maxwellian. This question has been addressed by Liao et al. (2015), who showed that only in the extreme cases of departure from the half-Maxwellian case are there visible differences in the gas flow field close to the nucleus surface.

Some aspects need to be addressed in specifying the boundary conditions. The temperature of the gas at the source is essentially unknown, which results in a significant number of free parameters for the initial boundary problem. From simple physical considerations and for simplicity, the outgassing rate for each facet is obtained from a simple energy balance equation (Eq. (1)).

$$\frac{S(1-A_H)}{r_h^2}\cos(i) = \epsilon\sigma T^4 + Z(T)L. \quad (1)$$

[1] http://www.plasmati.tw.

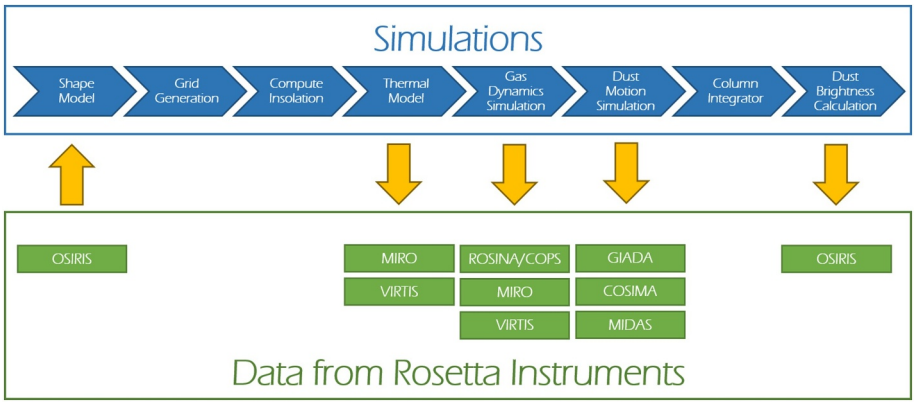

Fig. 1. Forward simulation and interactions of Rosetta data sets (after Marschall et al., 2017).

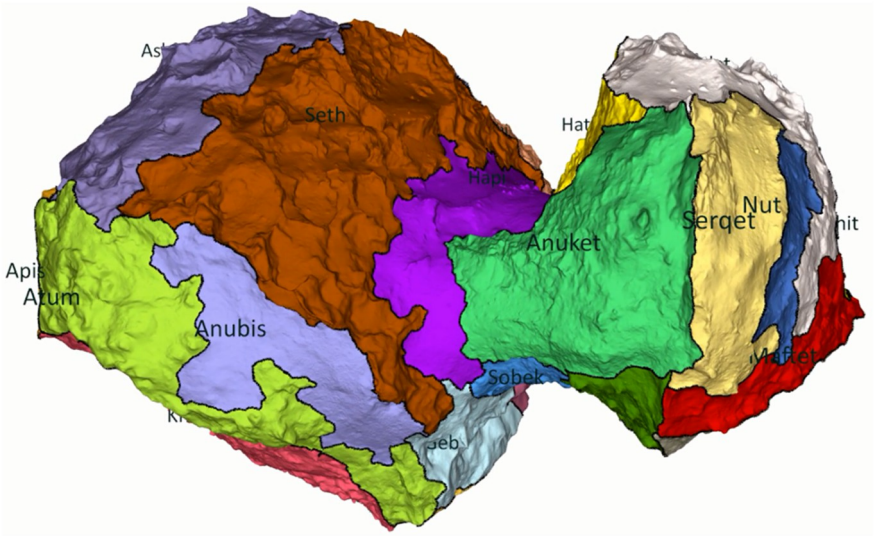

Fig. 2. One view of the SHAP7 shape model highlighting the morphological regions.

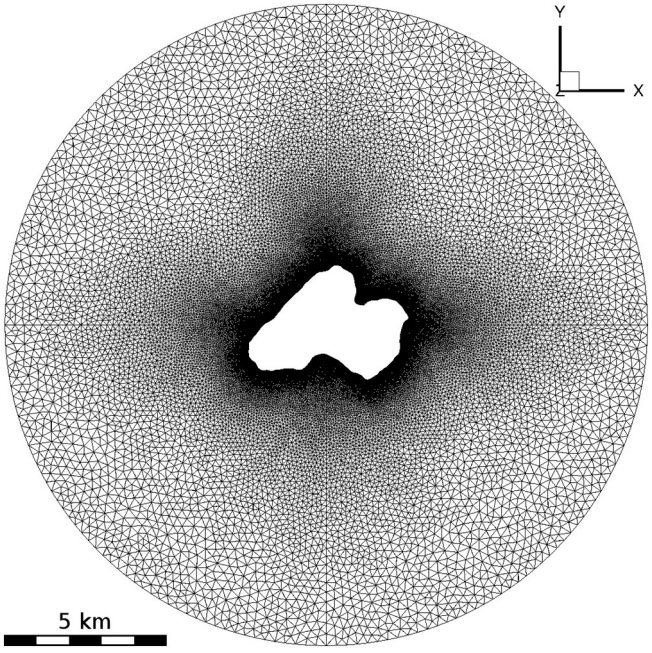

Fig. 3. An example of a slice through the unstructured grid with over 13 million computational cells developed for the gas dynamics simulations.

The left hand side of Eq. (1) denotes the solar irradiance inversely proportional to the square of the heliocentric distance, r_h, and proportional to cosine of the solar incidence angle, i, and the solar constant, S, at 1 AU (taken to be 1384 W m^{-2}). A_H is the directional–hemispheric albedo (set to 0.04, Fornasier et al., 2015). On the right hand side we have the thermal re-emission term proportional to the surface temperature, T, to the fourth power, the Stefan-Boltzmann constant, σ, and emissivity, ϵ, and also the energy loss due to sublimation as a product of latent heat, L, and sublimation flux, $Z(T)$. For L_{H_2O} we adopt a value of 2.84×10^6 J/kg (Huebner et al., 2006) which leads to a maximum sublimation temperature of approximately 200 K. Under the stated assumptions, the surface temperature would be in fact the sublimating ice temperature, and the energy balance takes place instantaneously. For the boundary conditions we do take into account effects of nucleus self-shadowing (projected shadows).

From thermal observations it is known that the thermal inertia of the cometary surface - at least on large spatial scales - is low with values in the range of 10–60 $Jm^{-2}K^{-1}s^{-\frac{1}{2}}$ (Gulkis et al., 2015; Schloerb et al., 2015; Choukroun et al., 2015). A value of 50 $Jm^{-2}K^{-1}s^{-\frac{1}{2}}$ fits most of the Rosetta measurements (Marshall et al., 2018). This implies that, for most cases, energy balance is established relatively quick (minutes) so that the sublimation rate can be computed without including thermal conduction into the comet's interior. Even more sophisticated models with ice mixtures (e.g. Marboeuf et al., 2012) show that such assumption is sufficient except a near-terminator activity. Nevertheless, Bieler et al. (2015), Marschall et al. (2016), and Fougere et al. (2016) have all

shown that ROSINA observations of the gas density at the spacecraft (Hässig et al., 2015) cannot be explained by a purely insolation-driven outgassing from a uniform nucleus. In other words, some surfaces outgas more strongly than others under the same illumination conditions. Furthermore differences between individual species, H_2O, CO, CO_2, and O_2, hint at the same fact (Hässig et al., 2015; Fougere et al., 2016).

Using a pure ice surface results in production rates that are far in excess of the densities observed by ROSINA (Marschall et al., 2016). Furthermore only very little ice was observed on the surface by VIRTIS (Raponi et al., 2016). Therefore the production rates need to be scaled down from that of a pure ice surface. We do this by the introduction of a free parameter we call the effective active fraction (EAF). The EAF can be thought of as the areal fraction (akin to a checker-board pattern) of a surface facet that is pure ice and can in principle be set individually for each facet. In practice though we only vary the EAF on a regional basis as explained later. This is done to reduce the number of free parameters to only a few rather than thousands. We should stress that the EAF has no direct physical interpretation but rather is a parametrization of the ice content of the surface. Whether the EAF of a certain area is lowered due to e.g. areal mixing of icy and volatile-free areas unresolved by the used shape model or by a dust cover cannot be determined here. But the EAF does give us a precise measure of the response of the surface to the energy input and how that translates to the production of outflowing gas. For this work we will be comparing the gas and dust flows resulting from two different maps of the EAF to the data of the different Rosetta measurements.

2.4. Computation of the gas and dust flow field

Once the surface boundary condition is specified, the DSMC code can be run. The code also allows different species to be emitted at different temperatures and has been tested with H_2O and CO_2 combinations. From the simulation's point of view, apart from initial density and temperature for individual facets, the surfaces can also be set to absorb or reflect impacting molecules. In this work we have set illuminated surfaces to diffusely reflect gas molecules and facets shadowed to absorb molecules. This approach follows the work shown in Marschall et al. (2017).

Once the gas flow field has been evaluated, the dust flow field calculation may begin. We use a typical approach for computing dust motion in a gas flow-field taking into account gas drag and the comet gravity as detailed in Marschall et al. (2016) and references therein. We assume that the dust mass production rate is proportional to the gas mass production rate and that the dust size distribution does not vary across the surface except in cases where certain dust sizes are no longer lifted because the gas pressure is too low to surpass the local gravity. The dust-to-gas mass production rate ratio and the dust size distribution are not independent as shown in Fig. 12 in Marschall et al. (2016). For a power law exponent of -2.5 a dust-to-gas production rate ratio of ~ 1.5 follows from the constraint of the brightness of the dust coma in the OSIRIS images. This low dust-to-gas production rate ratio in conjunction with the rather flat size distribution also implies that the momentum transfer from the gas flow to the dust particles is negligible in our cases, and therefore, can be safely neglected. We assume the particles to be spherical with no initial speed at the surface with the same density as the bulk density of the nucleus (538 kg m^{-3} Preusker et al., 2017). Because no ejection mechanism is yet known we consider cohesionless particles at the surface.

2.5. Column integrator

A simple column integrator is used to determine the gas or dust column densities for comparison with remote sensing observations using the position of the spacecraft derived from SPICE kernels (Acton, 1996) produced by ESA. It is important to recognize that extrapolation outside the simulation domain is sometimes necessary and is performed by using a $1/r^2$ law (both in the case of calculating gas column densities along a line of sight e.g. for VIRTIS-M-IR and dust column densities for OSIRIS comparisons). Following work by Marschall et al. (2017) and Gerig et al. (2018), this seems to be a realistic assumption.

2.6. Dust brightness calculator

Knowing the distribution of dust particles - number density as a function of size - within the inner coma the scattered light intensity may be computed. Mie theory is adopted in the calculation of the scattered light intensity in the visible wavelength range, for comparison with the OSIRIS observations. A large fraction of the dust observations obtained remotely were acquired at intermediate phase angles (60–120°) where changes in the scattering function with phase angle are relatively small. Hence Mie theory is probably sufficient at this stage, although its deficiencies for application to irregular particles is acknowledged. Further information on the phase dependence is given in Bertini et al. (2017).

Dust brightnesses are computed with Mie theory using the algorithm of Bohren and Huffman (1983) under the assumption of zero optical depth. In total, 40 dust particle sizes are used from 8 nm to 300 µm. Separate images in each size bin can be computed to show differences in the behaviour of different particle sizes. Combining these images with different weighting allows us to test different particle size distributions against observations from the OSIRIS instrument (Marschall et al., 2016). Each dust size is weighted according to a power law dust size distribution as described in Marschall et al. (2016).

Thus the observed radiance, I, from the dust can be computed. For the single scattering approximation in the absence of optical depth effects (appropriate for 67P), the scattered radiance from the dust is given by

$$I = \int_{r_{\min}}^{r_{\max}} \frac{F(\lambda)}{r_h^2} n_{col}(r)\sigma_{geo}(r)q_{eff}(r)\frac{p(r,\lambda,\varphi)}{4\pi}dr \quad (2)$$

for a single particle type with the corresponding complex refractive index, where r is the dust particle radius, λ is the wavelength of the light, F is the solar flux at 1 AU, r_h the heliocentric distance in AU, n_{col} the dust column density, σ_{geo} the geometric cross-section of the dust grain, q_{eff} the scattering efficiency, and p the phase function for the scattering angle, φ. The scattering angle is defined as the angle between direction of the incident light and the direction of the scattered light.

3. Observations and data reduction

3.1. In-situ instruments

3.1.1. ROSINA

One of the instruments that provided key measurements was the Rosetta Orbiter Spectrometer for Ion and Neutral Analysis (ROSINA). ROSINA consisted of the Double Focusing Mass Spectrometer (DFMS), the Reflectron-Type Time-Of-Flight (RTOF) mass spectrometer, and the COmet Pressure Sensor (COPS) to measure the composition and total density of volatiles from in-situ, i.e. at the location of the spacecraft (Balsiger et al., 2007). Among other species (Le Roy et al., 2015) ROSINA measured the abundance of the major molecules, H_2O, CO_2, and CO (Hässig et al., 2015) throughout the active mission at the comet of more than two years.

The output from any DSMC code will give values for the gas density, velocity, and temperature. The density (and occasionally the velocity) can be compared with the in-situ measurements made by the ROSINA/COPS nude and ram gauges. The nude gauge densities have been compared to DSMC models in the past by Bieler et al. (2015) and Marschall et al. (2016). In the event that two or more species models are run, the relative composition determined by the mass spectrometers, DFMS and RTOF, can be combined with the COPS results to

produce partial densities for each species for comparison with the model. In the case of RTOF all species are measured at exactly the same time and can therefore easily be compared (Gasc et al., 2017). In the case of DFMS first the detector signal has to be interpolated in time as the different species are measured in sequential order: i.e. the spectra are obtained in sequential order, taking roughly 30 s per integer mass.

As described above our main free parameter is the effective active fraction (EAF) which essentially determines the spatial distribution of sources of gas at the surface. By means of varying the EAF we seek to minimise the difference between the model predictions and the ROSINA measurements. This feeds back into the assumptions of further models by means of analysing for which illumination and observation conditions the fit has improved. The best fit result of this iterative process which also includes measurements described below is presented in Section 4.

3.2. Remote sensing instruments

For some remote sensing instruments, the model outputs cannot be directly compared with the measurements, even in relatively simple cases (low optical depths). Probing of the major species in the coma can be performed at infrared wavelengths. The O—H symmetric stretch (in the absence of a deuterium atom) occurs at a wavelength of around 2.7 μm for the H_2O abundance determination. For CO_2 the asymmetric stretch occurs at 4.2 μm, and the CO molecule has a vibration-rotation transition centred around 4.7 μm. It is typically these three wavelengths that are targeted by infrared spectrometers such as VIRTIS (Coradini et al., 2007) to study the coma emissions of these major cometary species.

3.2.1. VIRTIS

The Visible and Infrared Thermal Imaging Spectrometer (VIRTIS) combines three data channels in one compact instrument to study nucleus and coma (Coradini et al., 2007). Two of the spectral channels are dedicated to spectral mapping (-M) at moderate spectral resolution in the range from 0.25 to 5.1 μm. The third channel is devoted to high resolution spectroscopy (-H) between 2 and 5 μm. The VIRTIS-H field of view is approximately centred in the middle of the -M image.

Bockelée-Morvan et al. (2015) presented method and results for estimation of gas column densities of H_2O and CO_2 in the coma of comet 67P using the VIRTIS-H (echelle type, 1.8 –5.1 μm, eight scattering orders) measurements covering the time span from Nov. 24th, 2014 to Jan. 25th, 2015. These data provide constraints because they can be directly compared with the simulated H_2O and CO_2 column densities within the VIRTIS-H field-of-view (FOV). Each VIRTIS-H data cube comprises hundreds of acquisitions. However, cube acquisition typically extends over several hours, a time span over which the geometry can change considerably because of comet rotation and spacecraft motion. This makes searching for spatially resolved variations in activity extremely difficult with this data set. This is the reason we do not present comparisons of our model with VIRTIS-H data in this paper but rather focus on VIRTIS-M-IR (below) with shorter cube acquisition times.

Assuming a fluorescence equilibrium (Bockelée-Morvan et al., 2015) the molecular band intensity, I, in the optically thin case, is related to the column density, N_g, through the equation

$$I = \frac{h\nu}{4\pi} g N_g \tag{3}$$

where ν is the central frequency of the band, h is the Planck constant, and g is the band emission rate (often referred to as the "g factor"). The g-factors for the infrared bands of the three major species have been given by Debout et al. (2016). The relative strength of the individual rovibrational lines depends on the gas temperature and hence the observed band structure (in high SNR VIRTIS-H data) can provide an additional constraint on the outflow.

The VIRTIS-M-IR instrument acquired spectrally resolved images (i.e. cubes) of the coma. VIRTIS-M-IR was an imaging spectrometer (1.0 –5.1 μm, 9.5 nm spectral sampling, spectral FWHM about 15 nm, 250 μrad × 250 μrad FOV per pixel; Coradini et al., 2007). Using the algorithm described by Migliorini et al. (2016) (continuum subtraction and emission band integration) the H_2O and CO_2 gas column densities for each pixel of each image recorded by the instrument have been determined. To increase SNR, some additional preprocessing steps had to be applied, including a spatial median smoothing and a 2 × 2-pixel binning of the cubes. We focus on a time span where the nucleus activity is already noticeable, until the VIRTIS-M-IR cryocooler failure in May 2015, and on cubes with a significant number of pixels sampling the coma. Although the SNR is significantly lower than for VIRTIS-H coma measurements, the latter provide gas column densities for only a single line-of-sight at a time or time span, whereas the VIRTIS-M-IR data enable the mapping of the spatial distribution of the gases. Taking into account that the different lines of a VIRTIS-M-IR image were acquired by scanning the scene with a movable mirror and thus at different times, we computed the viewing geometry for each pixel using SPICE as described above. This was then used to reconstruct the expected spatial pattern of the gas species from the model. For the cubes considered here, a basic acquisition typically has an exposure duration in the order of seconds, whereas the acquisition of the entire cube by scanning the scene with the scanning mirror took in the order of tens of minutes.

By comparing the column integrated results of our gas dynamics code to the VIRTIS-M-IR cubes we can constrain the relative strength of gas emission from different regions at the surface of the comet (as we show later). This is an additional complementary constraint to the one of ROSINA seen above. To quantify the goodness of the fit of different models to the measurements we calculate the χ^2 of column density profiles (as shown in the Section 4, Fig. 11). By means of feeding back missing features of the model compared to the observations into subsequent models the fits of the other instruments can also be improved.

3.2.2. MIRO

The Microwave Instrument for the Rosetta Orbiter (MIRO) consists of two heterodyne receivers: a sub-millimetre spectrometer operating at a centre band frequency of 562 GHz (0.5 mm); and a millimetre spectrometer at 188 GHz (1.6 mm) (Gulkis et al., 2007). A Chirp Transform Spectrometer (CTS, Hartogh and Hartmann, 1990) is connected to the sub-millimetre receiver with 4096 channels and a spectral resolution of 44 kHz. Between 547 and 580 GHz, the water isotopologues $H_2^{16}O$, $H_2^{17}O$ and $H_2^{18}O$ can be observed, as well as carbon monoxide, ammonia and methanol. A spectrum is nominally collected every 30 s. The less abundant isotopologues are of particular interest when optical depth effects in $H_2^{16}O$ become significant, which was the case relatively early in the mission (Aug. 2014). The water lines have a large absorption cross-section. Hence observations looking at the nucleus and measuring the depth of the water lines in absorption has been found to be easier to interpret than observations off the nucleus when water lines are seen in emission due to inhomogeneities along LOS for such geometry (Lee et al., 2015). The resolved spectral lines shapes observed by MIRO also provide information on the bulk velocity of the gas. This makes the MIRO observations highly complementary to the VIRTIS measurements. The first results from the MIRO observations can be found in Lee et al. (2015) and Biver et al. (2015).

In this work we use nadir geometry observations for selected "events", covering the period from May 1*st* to 20 *th*, 2015. The events should be understood as 10–20 min averages of MIRO spectra such that the random component of measurement noise is less than about 3 K brightness temperature. One also has to make sure that all the individual pointings within the given averaging time interval do not undergo large changes (i.e. no pointing off of the nucleus - even partially, but we also check that the continuum temperature deviations remain < 5 K during averaging). Therefore, the events have been

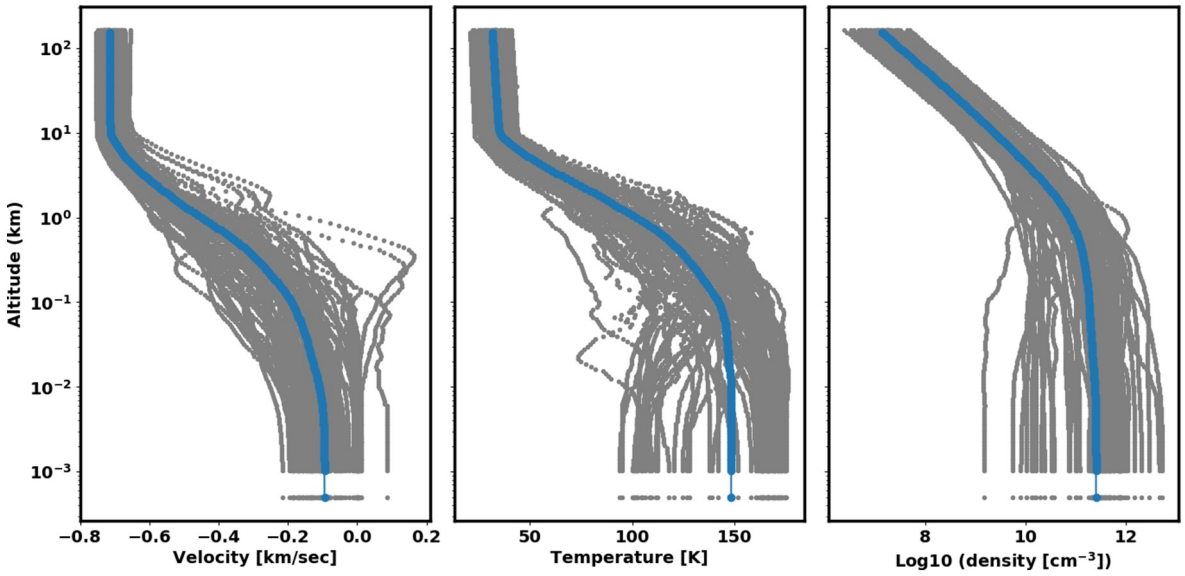

Fig. 4. The DSMC simulated profiles of velocity, temperature and water number density for the selected events from the MIRO database. The individual profiles are shown in grey circles with the averaged profiles plotted in blue. During this time period the spacecraft distance ranged from about 120 to 170 km (see text for details).

selected manually, providing 71 events in total. The DSMC model is used for each of the central time-stamps within the respective time bin for comparisons, and also as the initial profile in the inverse modelling. The simulated profiles for all the events are summarized in Fig. 4. It is interesting to note that even the model profiles extracted along the MIRO nadir LOS profiles do not exhibit radial expansion in a strict sense (due to the shape and roughness of the nucleus). This is manifested as a clearly discernible vertical structure in all three parameters up to 3–5 km altitude above the surface. The detailed discussion will be presented in Section 4.

To obtain water density (n_w), temperature (T_k) and velocity (v_{exp}) along the MIRO LOS direction we use an inversion procedure to simultaneously fit the $H_2^{16}O$ and $H_2^{18}O$ line shapes of the ortho-water ground transitions. For convenience and brevity we will refer to the LOS n_w, T_k, and v_{exp} as "altitude profiles". To calculate the simulated MIRO spectra we rely on a 1D radiative transfer code accounting for non-local thermodynamic equilibrium (non-LTE) effects in the line excitation using the same non-LTE model as in Lee et al. (2015), Biver et al. (2015), and applied in Marshall et al. (2017). The non-LTE effects are not generally very pronounced for the selected events due to higher activity of the comet in May 2015, and selection of events that favour daytime conditions. LTE conditions generally hold from about 40 to above 100 km altitude (for the typical water column densities from 10^{15} to 10^{17} [molec. cm^{-3}] observed during this period).

In this work we adopt a two step retrieval procedure. The first step is a brute force search, a single parameter scaling, for the input water density profile, while the measured, y_m, and simulated, y_c, spectra differences keep decreasing. This way we ensure in an automatic manner that the initial water density is not over-estimated as is the usual case for model profiles. In the second step, we apply an iterative damped least-squares algorithm, sometimes called the Twomey-Tikhonov regularization method (Rodgers, 1976; Menke, 1989), to simultaneously obtain profiles of n_w(z), T_k(z), and v_{exp}(z). The mathematical formalism is actually equivalent to the widely used "optimal estimation" (OE) (Rodgers, 1976; Eriksson, 2000) both in Earth and solar system atmospheres, the difference being only in the interpretation of the regularization matrix (a-priori covariance matrix). The least squares procedure minimizes the weighted sum of the L_2 norm of prediction error and solution simplicity:

$$Min.: \quad [\mathbf{y_m} - \mathbf{y_c}]^{\mathbf{T}}\mathbf{S_e^{-1}}[\mathbf{y_m} - \mathbf{y_c}] + \alpha[\mathbf{x} - \mathbf{x_a}]^{\mathbf{T}}\mathbf{W^{-1}}[\mathbf{x} - \mathbf{x_a}]. \tag{4}$$

The vector $\mathbf{x}$ is the quantity we seek to retrieve and contains altitude discretized n_w(z), T_k(z), and v_{exp}(z). x_a is the (a-priori) vector, our best estimate before the measurement, and is weighted by the regularization in cases where the measurements do not provide enough information for the desired parameters. We find that 15 points for density profile (converted to logarithm during inversion) and 30 points for T_k(z) and v_{exp}(z) provide enough freedom to fit the measured data and keep the inversion stable for the different profiles. The $\mathbf{S_e}$ and $\mathbf{W}$ are weight matrices with measurement noise (diagonal, with estimated random radiometric noise) and regularization matrix (a-priori covariance)[2] respectively. The regularization matrix (or a-priori covariance matrix) contains off-diagonal elements that correlate parameters at different heights. We follow the expression from Rodgers (2000)

$$\boldsymbol{W}(ij) = \sigma_i \sigma_j \exp\left(-\frac{|r_i - r_j|}{L}\right), \tag{5}$$

where r_i denotes the altitude at a grid point, σ_i is the standard deviation for the a-priori profile at the point r_i and L is the characteristic height scale. Alternatively, we also tested Gaussian and triangular forms of the correlation functions. As it turns out the exact form of the correlation function plays only a little role, since both σ and L are determined empirically.

The α parameter denotes a relative weighting of the two terms and is usually chosen by trial and error, but it is often subsumed into the W matrix. The iterative procedure minimizing (4) solves the following equations

$$(\mathbf{K^T S_e^{-1} K} + \mathbf{W^{-1}})\Delta\mathbf{x} = \mathbf{K^T S_e^{-1}}(\mathbf{y_m} - \mathbf{y_c}) - \mathbf{W^{-1}}(\mathbf{x} - \mathbf{x_a}) \tag{6}$$

$$\mathbf{x_{i+1}} = \mathbf{x_i} + \Delta\mathbf{x}. \tag{7}$$

An important diagnostic quantity is the Jacobian matrix, $\mathbf{K}_{nm} = \frac{\partial y_n}{\partial x_m}$, showing the sensitivity of radiance at frequency, n, to the parameter, m. In essence, it illustrates from which altitudes we have sensitivity to the measured spectrum at frequency, n, from a parameter, m. An example (for the $H_2^{16}O$ transition) is shown in Fig. 5, for one of the 3D DSMC calculated profiles. The plotted Jacobians (rows of the $\mathbf{K}_{nm}$) allow us to understand at which altitudes we expect the largest sensitivity to the parameter of interest and also indicate how well we can resolve the altitude profile. For example, we can see that there are almost no peaks

[2] This would be S_a^{-1} in the context of (Rodgers, 1976, 2000).

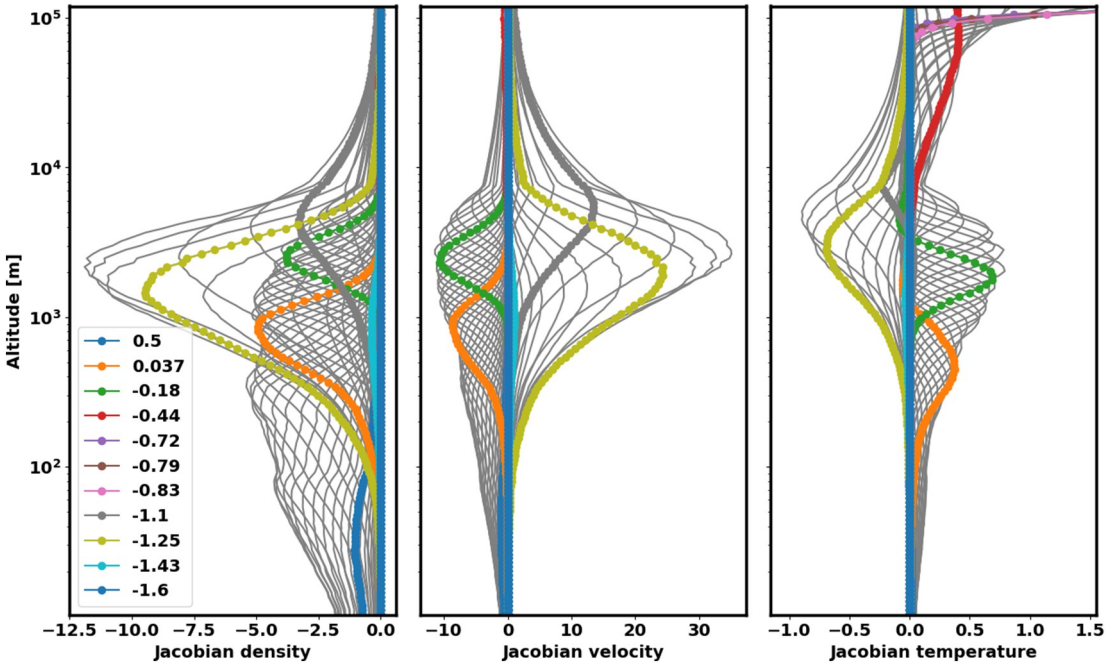

Fig. 5. The three panels show the Jacobians for the $H_2^{16}O$ line with respect to density, expansion velocity, and temperature for a a typical example of calculated profiles from the DSMC code. The lines in colour show rows of the Jacobian matrix for selected velocities (frequencies) shown in labels in units of [km/s] (in this example the line centre is at about −0.72 km/s). The abscissas are shown in arbitrary units.

of the velocity Jacobians below ~400 m or above ~8 km. This means that in those regions we can obtain only weighted averages (very coarse altitude resolution), as intuitively understood from the physics of the line formation in expanding atmospheres. One should keep in mind that $\mathbf{K}_{nm}$ is in fact a function of **x**, and hence depends on the actual profile shape. In addition, we note that the T_k Jacobians do show some degree of separation of peaks of the functions all the way up to 100 km (the line core shows large sensitivity toward the highest altitudes, as this is an optically thick line). The n_w Jacobians show a good sensitivity for the nadir geometry in the range of 50–100 m to ~ 10 km. In all cases the abrupt change of the functions into a constant value at the ~10 km altitude is due to constant extrapolation of the DSMC profiles up to the altitude of the simulated sensor. Similarly, the code relies on the Jacobians of the $H_2^{18}O$ transition, which look similar in shape and altitude of the peak sensitivity to the $H_2^{16}O$ Jacobians. Naturally, the $H_2^{18}O$ transition is less optically thick (but not opt. thin) for the simulated time period. This means that the optically thick line yields high sensitivity to the temperature profile retrieval while the velocity estimation relies more on the information from the $H_2^{18}O$ line. Nevertheless, the simultaneous retrieval treats this information simultaneously and numerically to satisfy the minimization conditions, i.e, Eq. (4). As will be discussed in the results section, the algorithm is able to fit the measured spectra to within measurement uncertainties in more than 90% of cases. The uncertainty analysis will be also presented later in Section 4.3.

3.2.3. OSIRIS

A further observable is the dust brightness distribution in the inner coma obtained by OSIRIS (Keller et al., 2007). These data have been accurately calibrated (Tubiana et al., 2015) and, in combination with Eq. (2), provide a constraint on the total dust loss and the spatial distribution of emission from the surface. Gerig et al. (2018) have illustrated how these data can also be used to assess the dynamics of the outflow. While the observations are not at a fixed cadence and usually acquired for specific objectives in the form of sequences, the complete data set provides a reasonably continuous record of the 2D radiance from the dust over the study period. Data were acquired for varying illumination conditions of the surface and changing viewing geometries. We use these data at specific times to constrain the models. As it is generally assumed that the dust is closely linked to the gas emission and coupled to the gas flow in the acceleration regime, the dust is a good tracer of the gas flow. Hence the dust not only acts as a constraint on the dust flow itself but additionally as a constraint and check of the gas emission.

Due to the complex dust dynamics within the first kilometres of the surface, the main goal of the synthetic images our model provides is to reproduce the dominant features seen in the OSIRIS data and thus understand the dominant physical processing resulting in different types of dust filaments in the inner coma. In particular, we have focused on the sequence of images taken by the OSIRIS wide angle camera (WAC) on 2018-05-05 and will be presenting the results of the model comparison in Section 4.4 by highlighting three of the images representative for that sequence. For each image and gas model we have run 40 different dust sizes ranging from 8 nm to 300 μm. The results of the different dust sizes are then convolved with a power law size distribution and converted to synthetic OSIRIS images in units of spectral radiance. These three images demonstrate 1) the need for an inhomogeneous gas activity distribution at the surface (EAF) resulting in an inhomogeneous dust distribution in the coma for a good first order fit, 2) the observation of slow moving particles originating from the Imhotep region, 3) insolation variations and local topography are sufficient for the production of most of the seen dust filaments for a good second order fit, and 4) enhanced dust emission from the Ma'at d) subregion (Thomas et al., 2018) that could not be resolved by the gas instruments.

4. Results and discussion

Previous work has investigated the period between Sep. and Nov. 2014 (Marschall et al., 2017, 2016). In this earlier work, the EAF was exhaustively iterated to provide a good fit to the ROSINA/COPS data. This was compared to a case where the EAF was constant over the whole object. In these cases, however, the imaging data for the southern hemisphere had not yet been fully incorporated into the shape model. Here, we use the most complete shape model data to determine the

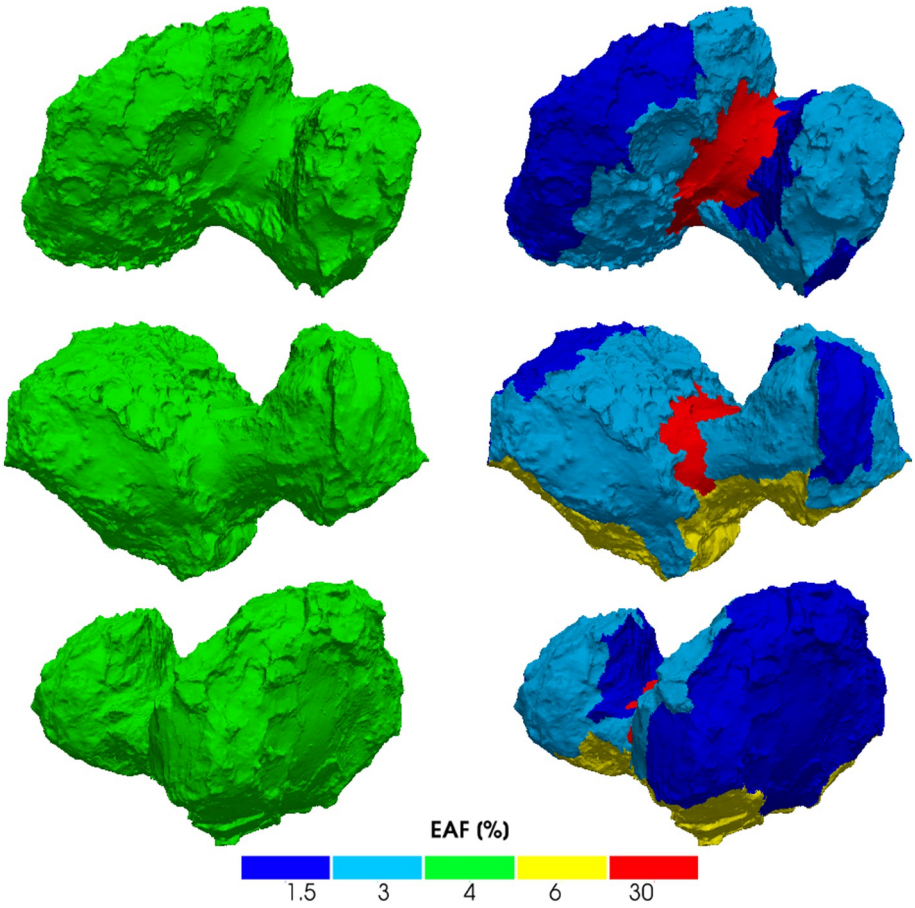

Fig. 6. The effective active fraction (EAF) for the two models to be compared with multiple datasets. The left column shows two views of the nucleus EAF and is for the insolation-driven model in which the EAF is a constant over the whole nucleus. The right column shows the inhomogeneous case where the EAF is varied regionally.

EAF.

In Fig. 6 the EAF for the two models are shown. On the left, the insolation-driven model shows a constant EAF over the whole nucleus. On the right, an inhomogeneous model for the EAF is assumed. In each case three views are shown for context. The EAF in the northern hemisphere is based upon the work of Marschall et al. (2017) yet has been slightly modified. By running many different models varying the regional strength of the emission for different regions the presented model provides the best fit to the different data sets simultaneously. As the solutions are non-unique this does however mean that this is likely not the only distribution that can provide a good fit. The Hatmehit and Imhotep regions of the nucleus are less active than the rest. The Hapi region has a high EAF. All the southern hemisphere regions (e.g. Wosret) have been set to one value that is intermediate. A direct comparison of these EAF maps with Marschall et al. (2017) will show that, for the northern hemisphere regions, the EAFs all have to be increased by a factor of 3. This was found to be necessary to match the ROSINA/COPS densities. Hence, there was a rise in activity between November 2014 and May 2015 that was larger than expected from free sublimation from a fixed area of water ice. Furthermore we have found that compared to the previous maps found for September–November 2014 the current maps require a low EAF for Hathor.

The way the best fit model was achieved was by means of iterating the EAF maps. We start with our benchmark model, the purely insolation driven model. The EAF of different regions are then varied and the results tested against the different data sets. Because not all instruments are sensitive to the same changes, different measurements confirm or rule out certain assumptions of the EAF. Though we have run many different regionally inhomogeneous models the one presented here represents the best fit.

All data sets will be compared to the gas and dust flows resulting from the maps of the two models. Fig. 7 shows the global production rate as the comet rotates for the two models at equinox on the 2015-05-10 when the comet was at a heliocentric distance of 1.67 au. The two curves significantly differ for most of the rotation even showing opposing trends. Compared to the purely insolation-driven model the regionally inhomogeneous model predicts for certain illumination conditions only half the global production rate, but up to 20% more flux for other conditions. These values are on the same order of magnitude as presented by Hansen et al. (2016) ($\sim 30 - 60\,\mathrm{kg\,s^{-1}}$). We should state that although we are confident in the overall magnitude of these numbers, one should keep in mind that we rely on a rather idealised

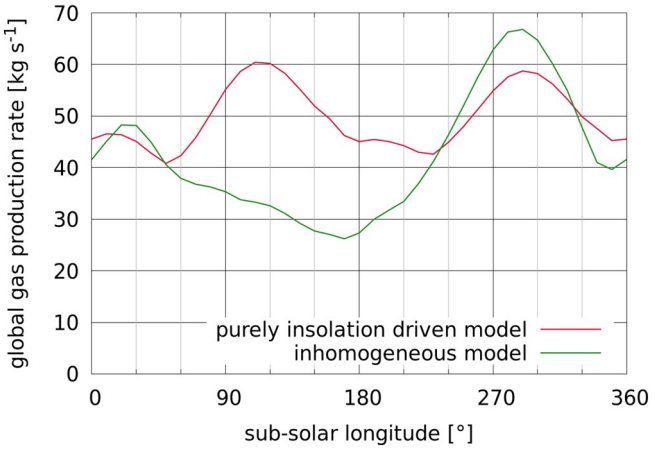

Fig. 7. Global gas production rate resulting from the two EAF maps in Fig. 6 on the 2015-05-10 when the comet was at the inbound equinox and a heliocentric distance of 1.67 AU.

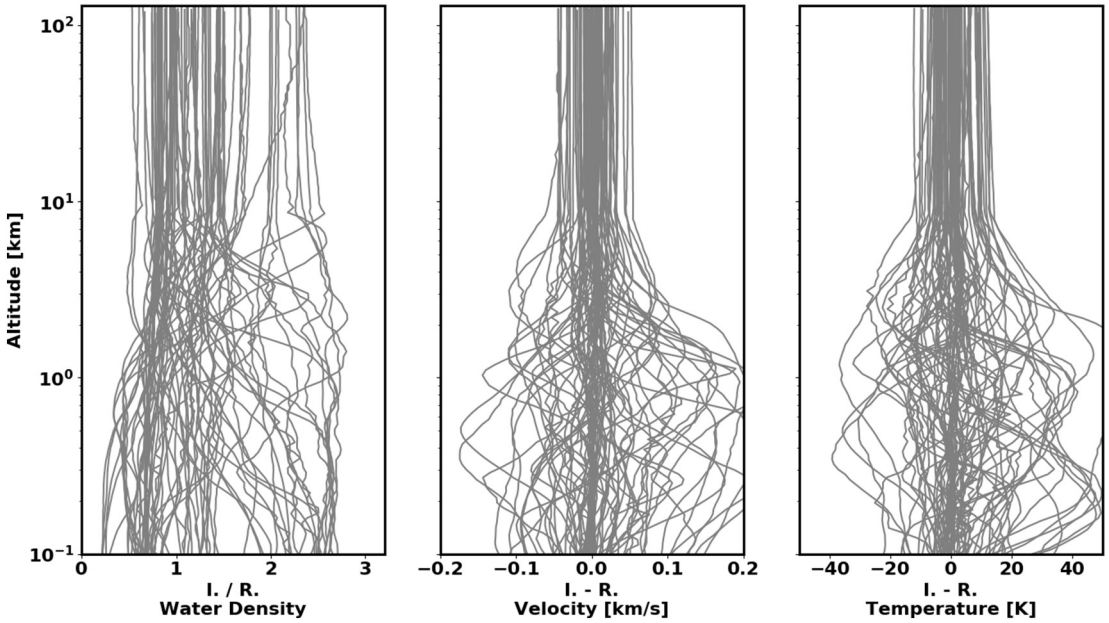

Fig. 8. The differences in the input profiles used for MIRO inversion between the pure insolation (I.) and regional (R.) (inhomogeneous) cases. The left panel shows the ratio for water density, the middle panel shows the velocity difference, and the temperature difference is shown on the right. There is significant difference in vertical structure of all three profiles in most cases below 10 km altitude.

thermal model. Furthermore, it has become clear from publications of other authors (e.g. Fougere et al., 2016; Zakharov et al., 2018) that different source distributions constrained mainly by ROSINA data can lead to good fits of the data. This is a result of the physics of the expanding gas which causes inhomogeneities at the surface to efficiently be smoothed over the first kilometres above the surface. This results in non-unique solutions with different global production rates. In that sense the values stated above should be understood with some caution. The differences between the two cases of EAF also result in significant differences in the inferred inner coma properties as demonstrated in Fig. 8. This figure shows the difference between the two models for the local gas properties along the MIRO line of sight from the spacecraft down to the surface.

Next, we describe in detail the results of comparisons with data acquired by ROSINA, VIRTIS, MIRO, and OSIRIS for the equinox 2015 period.

4.1. ROSINA comparisons

Comparisons with the ROSINA data constitute our first model benchmark. ROSINA produces a very accurate, albeit local measure of the gas density and its variation with time at the position of the spacecraft. Fits to these data are already becoming very sophisticated (Marschall et al., 2017, 2016). For the data acquired in November 2014, optimization of the fit has been performed by modifying the EAF on the nucleus. A statistical approach was used by Marschall et al. (2017) to show that solutions are strongly non-unique. However, purely insolation-driven models could be distinguished from inhomogeneous models, and hence ROSINA provides a meaningful constraint as a starting point for further comparisons. The insolation-driven model could be rejected for the November 2014 time-frame, and it was shown that higher emission from the Hathor and Hapi regions and low emission from most of the rest of the nucleus were consistent with the ROSINA data.

In Fig. 9, we see a comparison between model calculations (green and red dots) and the ROSINA/COPS data (blue dots) for the May 2015 period. The model was run for eight orientations of the nucleus with respect to the sun with sub-solar longitudes of 0°, 45°, 90°, 135°, 180°, 225°, 270°, and 310°. Then the density at the spacecraft position was extracted for these illumination conditions. The error bars on the model represent the statistical errors from the DSMC code. Neither model gives a perfect fit to the data but the green dots (representing the inhomogeneous case) provide a better fit when the sub-spacecraft point is above intermediate latitudes (from 2015-05-06 to 2015-05-10). Because it is difficult to judge from Fig. 9 which model performs how well compared to the measurements we have calculated the relative difference[3], Δ, between the measurements and the two models for the shown period. For the purely insolation-driven model the relative difference is 33.6% and for the inhomogeneous model it is 27.6%. While the inhomogeneous model performs better the difference is not very large and thus ROSINA does not provide an unequivocally strong preference between the two models. The insolation-driven model shows the largest absolute deviations at this time. The maxima are coming from Imhotep in the insolation-driven case. Deviations from the data for both models after 2015-05-09 are in general < 40%. On this basis, there is little to choose between the two models with the exception being that Imhotep cannot be a significant insolation-driven source with the same EAF as elsewhere. Hence ROSINA does not provide a strong constraint for the source distribution of the models during this period.

4.2. VIRTIS comparisons

Migliorini et al. (2016) derived H_2O and CO_2 gas column densities from VIRTIS-M-IR spectra measured between April 8th to 14th 2015.

We have used our DSMC code to simulate the 3D flow of H_2O emitted from the nucleus surface at discrete rotational phases and different mission times (as described above). By means of a column integration - on a pixel to pixel basis - through the gas coma we reproduce the viewing geometry and thus geometrically match the VIRTIS-M-IR data. These synthetic gas column density maps are directly compared to the measurements as shown in Fig. 10. The purely insolation-driven model reproduces to a large extent the emission from the ‘ Neck’ (Hapi) region but over-predicts the observed emission from the rest of the nucleus substantially. This indicates that most of the nucleus is only

[3] $\Delta = \frac{1}{N}\sum_{i=1}^{N}\frac{x_i - m_i}{m_i}$, where N, is the number of measurements, x_i is the model value, and m_i is the respective measured value

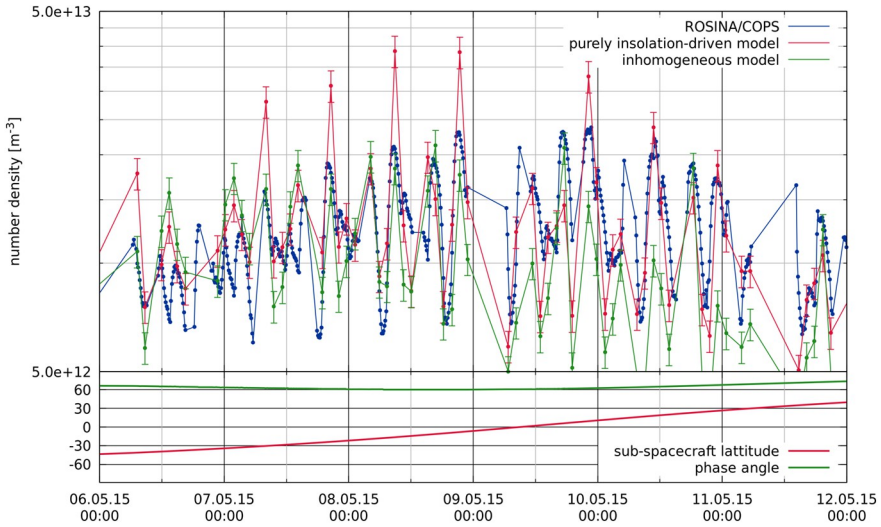

Fig. 9. Model fits to the ROSINA/COPS data (blue dots) with insolation-driven (red dots) and inhomogeneous models (green dots). The quality of the comparisons is in both cases reasonably good with the inhomogeneous distribution providing a slightly better fit to the data. The sub-spacecraft latitude and phase angle are shown in the lower panel.

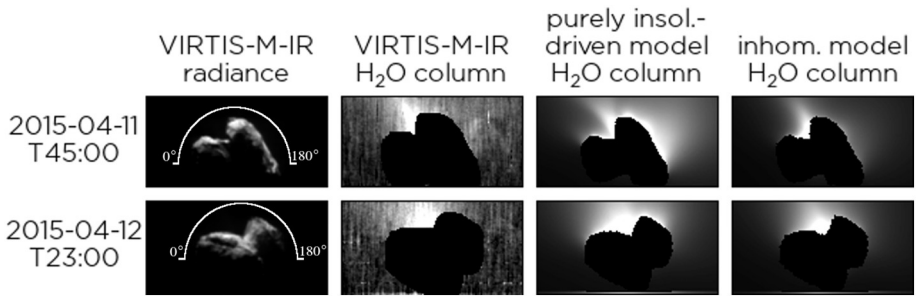

Fig. 10. Cubes a) and g) from Fig. 6 of Migliorini et al. (2016) are compared to our model. The top row shows cube a) data, and the bottom row shows cube g) data. The two left columns show the VIRTIS -M-IR radiance and the derived H_2O column density. The 3rd column shows the modelled VIRTIS-M-IR H_2O column density from the purely insolation-driven model. The 4th (rightmost) column shows the result from the inhomogeneous model.

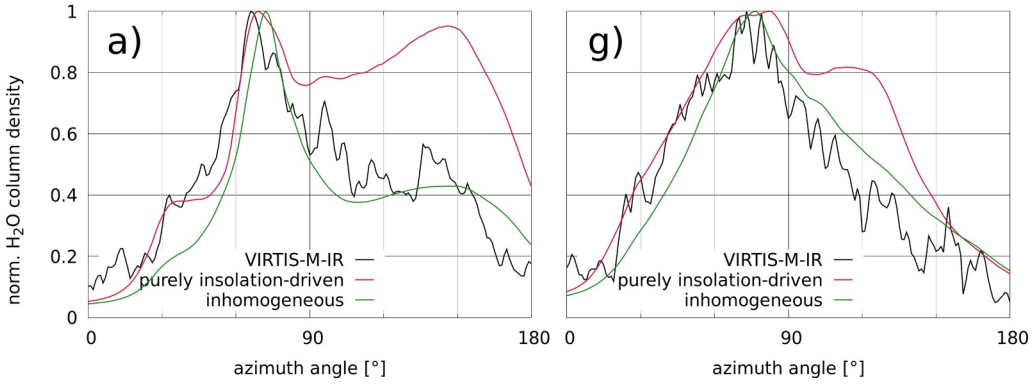

Fig. 11. Normalised gas column density as a function of the azimuth angle along the circle indicated in Fig. 10 for the VIRTIS-M-IR cubes (black lines) compared to the purely insolation-driven model (red lines) and the regionally inhomogeneous model (green lines). Cube a) shows the results for the cube in the top row of Fig. 10 while cube g) shows the results for the cube in the bottom row of Fig. 10.

very weakly active compared to the “Neck ”. This is especially clear when looking at the predicted emission from the Imhotep region (top right panel of Fig. 10) compared to the observed H_2O column density. In that panel Imhotep is located on the right edge of the nucleus silhouette. Compared to the emission from the “Neck” hardly any emission is visible in the VIRTIS-M-IR cube compared to substantial column densities comparable to the ones above the “Neck” in the purely insolation-driven model. From Fig. 11 we can quantify this behaviour in more detail by comparing the normalised gas column density as a function of the azimuth angle along the circles indicated in Fig. 10. For cube a) we see that the emission from Imhotep (peak at an azimuth angle of roughly 150˚) in the purely insolation-driven model is a factor of two higher than in the measured data while the inhomogeneous model matches the data well. For cube g) the differences between the two models are not easily seen in Fig. 10 while in Fig. 11 they are evident. The inhomogeneous model comes close to reproducing the data but the purely insolation-driven model shows a secondary peak at an azimuth angle of roughly 120˚ not represented in the measurements. For the profiles shown in Fig. 11 we have calculated the χ^2. The χ^2 of the purely insolation-driven model is 47.9 and 20.6 for cubes a) and g) respectively. For the regionally inhomogeneous model the χ^2 is 7.61 and 8.70 for cubes a) and g) respectively. This shows the much better fit of the regionally inhomogeneous model which confirms the qualitative assessment of Figs. 10 and 11. VIRTIS thus provides a much stronger constraint for this time period than ROSINA does. In particular we see a large improvement from the purely insolation driven to the regionally inhomogeneous model which - though the trend can be seen - is less clear from the ROSINA comparison. The behaviour shown in these two cubes can be observed also in many other studied cubes from this mission time. The examples shown here are representative of the situation.

We can thus conclude here that the VIRTIS-M data for H_2O have provided a telling constraint on the H_2O emission and strongly favours the inhomogeneous model over the insolation-driven model.

Table 1
Observing conditions for the five study cases.

Case	Date[a]	S/C[b] [km]	SZA [deg]	Region[c]
A	2015-05-04T18:00	149	42	Imhotep
B	2015-05-04T22:30	153	73	Sobek/Neith/Bastet
C	2015-05-19T01:30	155	68	Ma'at
D	2015-05-20T10:00	170	42	Imhotep/Ash

Notes.
[a] Time of mid-point observation.
[b] Is the cometocentric spacecraft distance.
[c] Approximate region(s) for the projected MIRO FOV. The solar zenith angle (SZA) represents the average value for all facets within the beam.

Furthermore, the profiles in Fig. 11 show that the model gives much smoother curves than seen in the data. Further data analysis should be done in the future to determine which of the variations are due to measurement noise and which are additional features the models did not capture.

4.3. MIRO comparison

Using the inversion approach described in the previous section we retrieved the n_w(z), T_k(z), and v_{exp}(z) profiles along the LOS for a specific MIRO observation (71 profiles in total). We should note that profiles of v_{exp}(z) will be shown with a negative sign for gas moving toward MIRO as projected along the LOS (expanding). It should be kept in mind that all vertical profiles are only projections along the LOS of MIRO beam, and not necessarily radial profiles.

This is the first time that this approach has been applied, allowing an appropriate fit to the MIRO measurements. We will first focus on several interesting case studies characterized by the viewing geometry (see Table 1 for details), and then provide a summary of results in a statistical manner. We will also discuss the differences between retrievals relying on regional versus purely insolation-driven model profiles used as initial guesses for the optimisation iteration.

First, we select a typical retrieved profile, *case A*, which occurred at a simple viewing geometry (sounding the Imhotep region). The results for *case A* are shown in Fig. 12, and we use this case to describe a few interesting features that are common in all retrieved cases, and also discuss the estimated uncertainties. The panels in Fig. 12a show spectra measured by MIRO (black line), calculated from the initial profiles supplied by the DSMC (blue), and then the final best fit spectra (red) for the solution of the inverse problem. All spectral lines are in units of Kelvin of antenna temperature (T_a). The inset in the top panel indicates the viewing geometry where facets in blue depict the MIRO beam size on the nucleus (using two times the beam width at 557 GHz). The bottom panel in Fig. 12a shows the difference between measured and synthetic spectrum for the final retrieved profiles. The retrieval achieves an excellent degree of fit, reproducing the line shapes within 2σ measurement errors. There are also several labels with diagnostics: *Vterminal* is the retrieved terminal velocity in the uppermost 20 km, *column-orig* and *column-fit* is the initial and retrieved profile column density respectively, and their *ratio* is also shown. However, there is a peculiar feature in the $H_2^{16}O$ transition (deeper absorption line) typically extending from 0.4 to 1.2 km/ s. There we can identify a weak emission spectrum, hence called the "red emission wing". This spectral feature being at positive velocities implies gas moving away from MIRO (in the context of random molecular motion), and also indicates gas being warmer than the background (sub-surface for sub-mm wavelengths). Hence, either the warm gas is emitted from the warmer visible surface with colder material below (indicating short thermal skin depth) or the gas is emitted sub-surface and heated on its way through the porous surface layer (Christou et al., 2018), although these are just proposed explanations that need confirmation by detailed modelling.

We do not force the algorithm to fit "red emission wing" feature, as the physics of its formation are still being investigated. The fact that this feature occurs for positive velocity would imply a gas moving away from the spacecraft very close to the nucleus, exactly where it should undergo rapid expansion. This feature is absolutely ubiquitous for the main isotopologue, it appears in nearly all measurements. The "red emission wing" feature looks very similar (though not as pronounced) when the MIRO beam happens to point partially off the nucleus, such that limb emission line is superimposed on the absorption spectra. However, this is definitely not the case in this example, considering the viewing geometry. Hence, there is probably physics connected to this spectral line feature. If the retrieval is fully "allowed" to reproduce the spectral feature (in this example), it would yield a very slow moving gas or stagnant layer of rather high temperature very close to the nucleus (below 400 m). The water density also may have to be enhanced, truly implying a stagnant layer decoupled from the expanding atmosphere. Another possibility is a 3D projection effect of the beam in an inhomogeneous coma. Nevertheless, this remains to be investigated and brought to a satisfying conclusion. In this work, this "red emission wing" is treated with less weight in the inversion procedure, such that the algorithm cannot obtain rigorous fitting at this time, hence affects the retrieved profiles as discussed.

The retrieved profiles for n_w(z), v_{exp}(z) and T_k(z) are shown in Fig. 12b from left to right as black lines with shaded regions representing the propagated random measurement errors into the solution (shown as 2σ). The blue lines show the initial (model) profiles. The y-axis represents the distance in meters from the comet surface (log scale), and we plot the profiles only above 50 m, as there is little sensitivity of measurement below these heights (see Fig. 5).

The total uncertainty, however, must take into account the fact that the problem may be non-unique and results may depend on the initial conditions. Therefore, we apply for each case the inversion starting from different sets of initial profiles, taken from the purely insolation-driven and the regionally inhomogeneous model results. If for a given time stamp of a MIRO measurement, observations within ± 2 h are available, we use their initial profiles for retrieval as well as for additional statistics. The results of quantifying the bias and variability due to different starting conditions are shown in Fig. 13. Bias (thick black line) is defined as average difference (or ratio for number density) between retrieved profiles obtained from different starting conditions, and variability is the standard deviation of this difference. On average the retrieval algorithm does not induce strong biases which are nearly zero for v_{exp}(z) and T_k(z), while the n_w(z) does show a bias profile on the order of 5–10 %. That means, starting with a larger density would yield a larger water estimate on average. The variability (shown as 2σ shaded region) due to different starting profiles in the inversion is a much larger component than the error due to measurement noise propagation and it is a strong function of altitude. The largest uncertainties for all parameters are below ~ 500–1000 m, and smallest at altitudes of 5 − 60 km. The temperature uncertainties do not grow even above 50 km, because of the optically thick $H_2^{16}O$ transition that provides good sensitivity. In summary, the water density profile has a large uncertainty, with a conservative estimate of a factor of two, while the velocity profile can be recovered with uncertainties of 20–50 m/s from 5 to 60 km and a little larger above these heights. The temperature can be rather well estimated from the spectra, within 20–30 K at all altitudes.

One of the interesting features in the retrieved T_k(z) profile shown in Fig. 12b are the sharply increasing values above 20 km altitude, peaking around 55 km height. Second, the T_k(z) profile has higher values than the one from the 3D model (for any of the two initial cases). Both of these features of the T_k(z) profile turn out to be present in most of the study cases, with only a few exceptions. We performed several numerical investigations of the retrieval algorithm to make certain that this is not a numerical artefact, and we are highly confident such a feature must be present to fit the spectral lines. In particular, the retrieved temperature gradients provide the correct shape of the $H_2^{16}O$

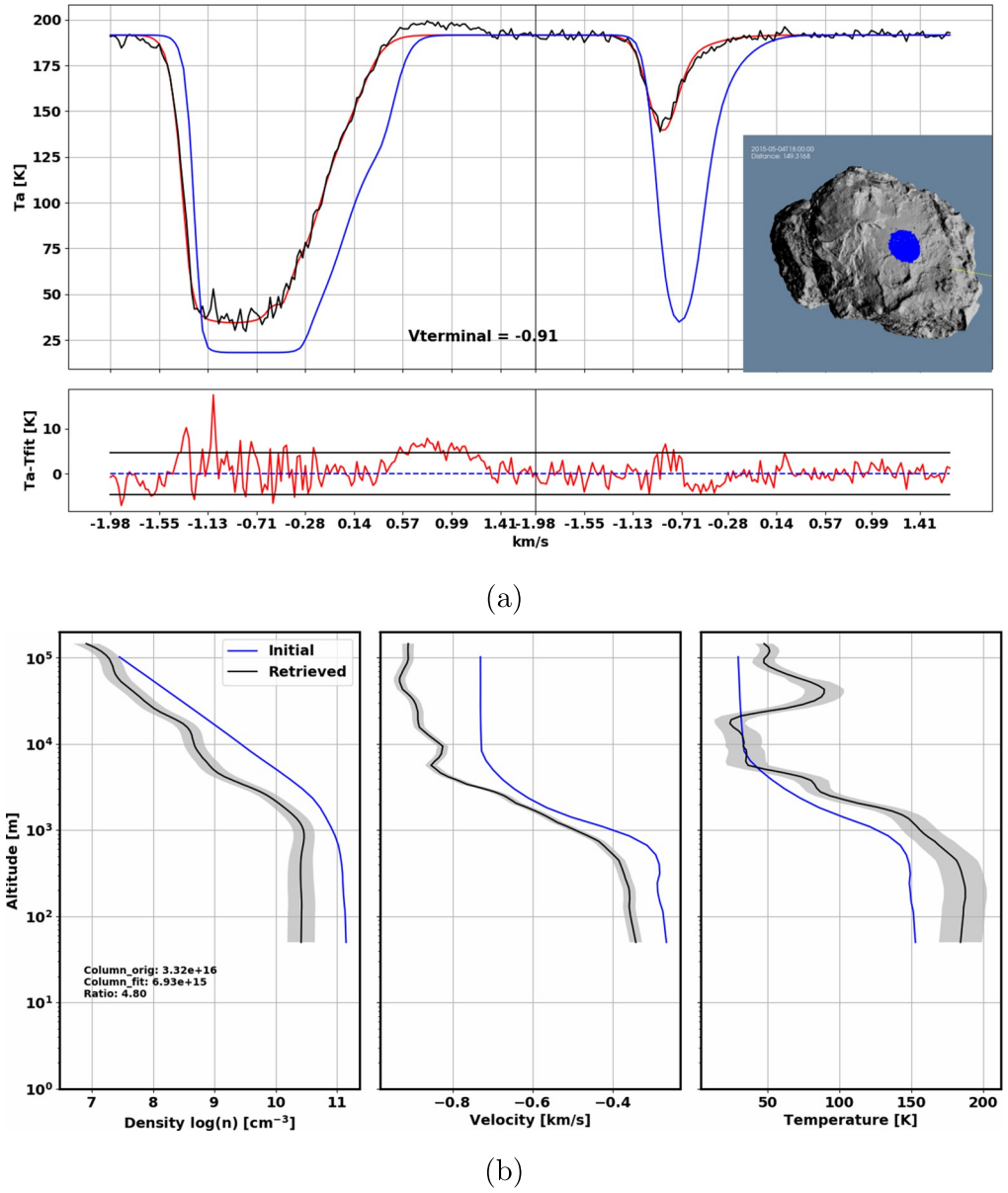

Fig. 12. (a) The top panel shows three spectra for the 557 GHz transitions of $H_2^{16}O$ (left) and $H_2^{18}O$ (right) for *case A* conditions: (black) MIRO measured, (red) synthetic after final iterations and (blue) synthetic at the first retrieval iteration. The bottom panel depicts the residual between measurement and best fit (red line). For most of the spectrum there is an excellent fit within 2σ of random measurement error shown as horizontal lines. (b) The three-panel plot shows vertical profiles of (left) number density, (middle) expansion velocity, and (right) kinetic temperature for starting conditions as blue lines, and final retrieved profiles as black lines. The shaded region represents a 2σ component of uncertainty due to measurement random error propagation. (See text for detailed discussion.).

spectral line near the line "core" as illustrated in Fig. 14.

In the left panel, the black and red lines show the MIRO measured and calculated spectra for the nominal temperature profile (red line in the right panel of the figure). When we force the T_k(z) profile to be constant above 19 km (blue-dashed) we immediately see that the match to the MIRO spectra (mainly the $H_2^{16}O$ line) is significantly worse. We also tried to force a constant T_k(z) profile above 44 km, but the fit to the MIRO spectra also suffers, especially around the -0.5 to -0.4 km/s region where differences (with the best fit) jump to about 8 K. Combined also with the steeper spectral slope around -1.4 km/s giving about 5 K of difference with the best fit, it is enough to keep the retrieval algorithm from converging properly. The $H_2^{18}O$ line shows much smaller effects in this example (at the level of measurement noise, ~3 K for the case shown in green). In summary, we did not find an altitude from where we can assumed a constant T_k(z) profile and still fit the MIRO spectra in this and other tested examples. In most of the cases the MIRO line shapes (especially the $H_2^{16}O$) imply a tendency of rising temperatures with height somewhere in the upper regions of the profile, usually above 20 − km but sometimes as high as 80 − km altitude.

Interestingly, the region where the T_k(z) shows heating of the coma, the velocity profile shows a decreasing velocity trend with absolute values comparable or exceeding the total 2σ uncertainty (as discussed above). However, this is much better seen in other cases discussed later. The *case A* shows a nearly constant altitude profile of expansion velocity above 50–60 km altitude. It is worth noting that any attempt to make a constant velocity profile between 1 and about 20 km cannot explain the MIRO spectra in any of the observations. The gas appears to be accelerating to high altitudes (as will be discussed later). Among the 71 profiles retrieved in the context of this study, observations of the Imhotep region yield the fastest gas velocities (larger than 0.9 km/s) although not the largest water column density.

Nevertheless, we cannot yet make a solid conclusion on the physical

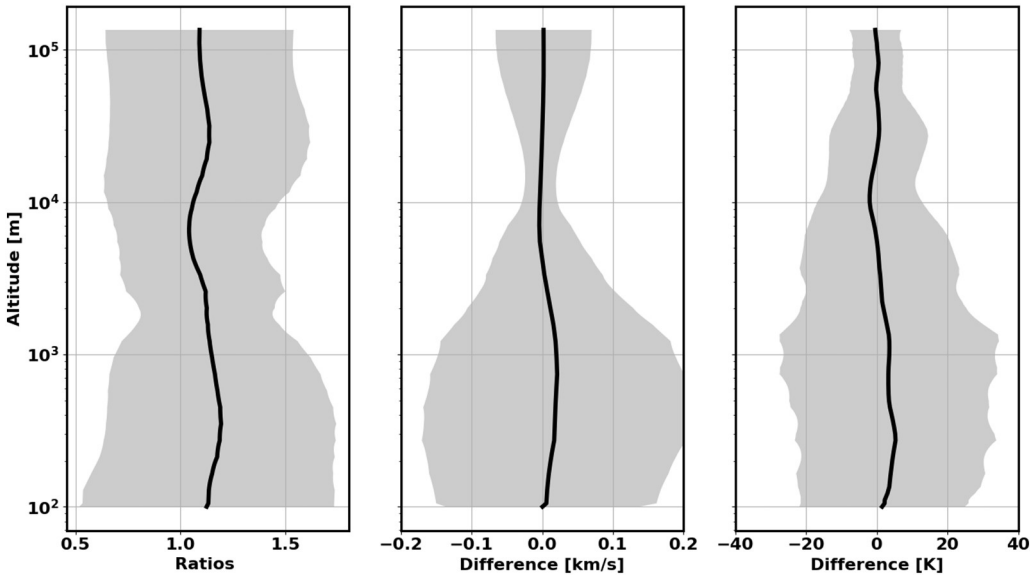

Fig. 13. Statistical determination of bias and variability due to different starting conditions in the retrievals. The thick black line is the bias, while the shaded regions represents 2σ variability. (Left) ratio of number densities (purely insolation-driven to regional inhomogeneous), (middle) velocity difference and (right) temperature difference.

cause for the detected warming at higher altitudes. As will be discussed in the summary, we can postulate hot electron impacts with neutral water, extended sublimation, etc, but the detailed analysis of the feature's local time, heliocentric and hemispherical variations should be quantified before this is possible. However, such analysis is beyond the scope of this paper. At the end of this section we also discuss how the absolute calibration of MIRO spectrometer data may limit the determination of the exact value of this "heating", which means that ultimately only statistical conclusions may have to be drawn, looking at this feature from a global point of view, rather than at individual profiles.

Finally we will discuss the retrieved n_w(z) profile (Fig. 12b). The MIRO measurements imply much smaller water densities than the DSMC model at all altitudes, leading to much smaller column density estimates. Despite the large uncertainty discussed above, this is a robust result with densities smaller by about a factor of 2 to 11 (in the most extreme case, not shown) compared to the DSMC model. The detailed fit to the MIRO spectral shape also reveals that the profile cannot be simply adjusted by scaling the model density. This may not be surprising since these are LOS measurements, not radial profiles, and despite the small beam of MIRO compared to the nucleus, different surface regions may contribute to the LOS.

Case B, shown in Fig. 15, is an example of a strong $H_2^{18}O$ absorption, one of the strongest in the 71 sample database, and this case also yields one of the largest water column density retrieved. The observation geometry and the MIRO FOV projected on the nucleus are shown in the inset of Fig. 15a. The "Neck" region, in this case on the southern hemisphere (Sobek/Bastet) usually shows large water densities, hence deep absorption lines for MIRO, although this is not a fully illuminated region (see Table 1), which is also indicated by the lower continuum (antenna) temperature of $T_a = 160$ K. *Case B* shows a stronger "red emission wing", and the algorithm, despite lower weighting, found a set of profiles that can explain this feature. Looking at the retrieved profiles in Fig. 15b, the velocity profile yields very slow expansion speeds below 300–400 m, and the gas kinetic temperature exceeds the measured continuum brightness by about 10–15 K. The "terminal velocity", which

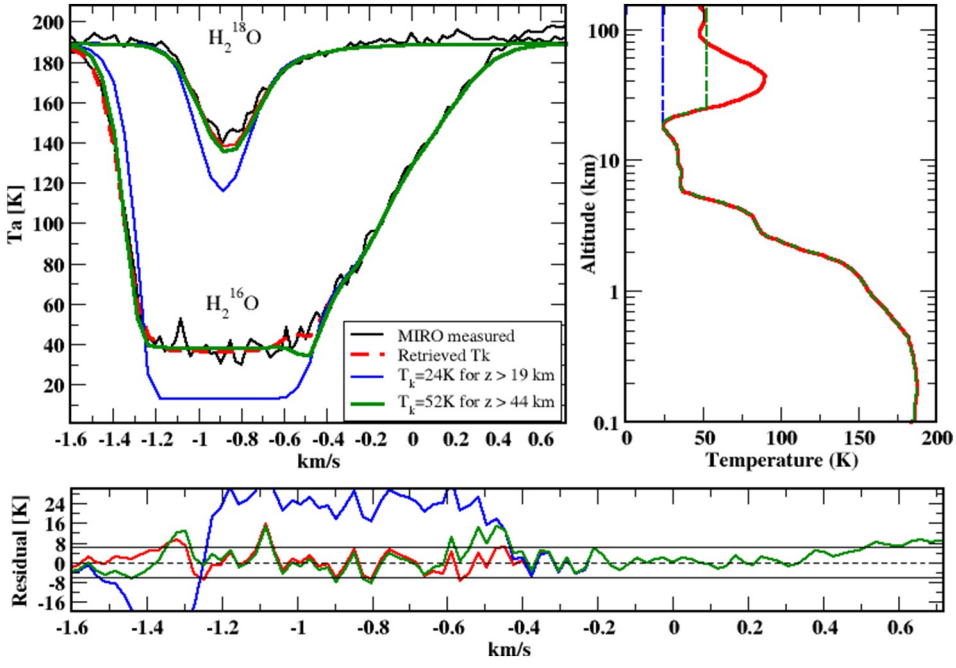

Fig. 14. An example showing the effect of a constant T_k(z) profile above different altitudes on the shape of the MIRO spectra. The example takes the same profiles and spectral line as in Fig. 12. The left panel shows a zoom-in on the spectra, while on the right the nominal (red curve) and the modified (green, blue) T_k(z) profiles are shown. At the bottom panel we show a residual of measured-calculated radiances for the $H_2^{16}O$ line, to easier follow the main text discussion.

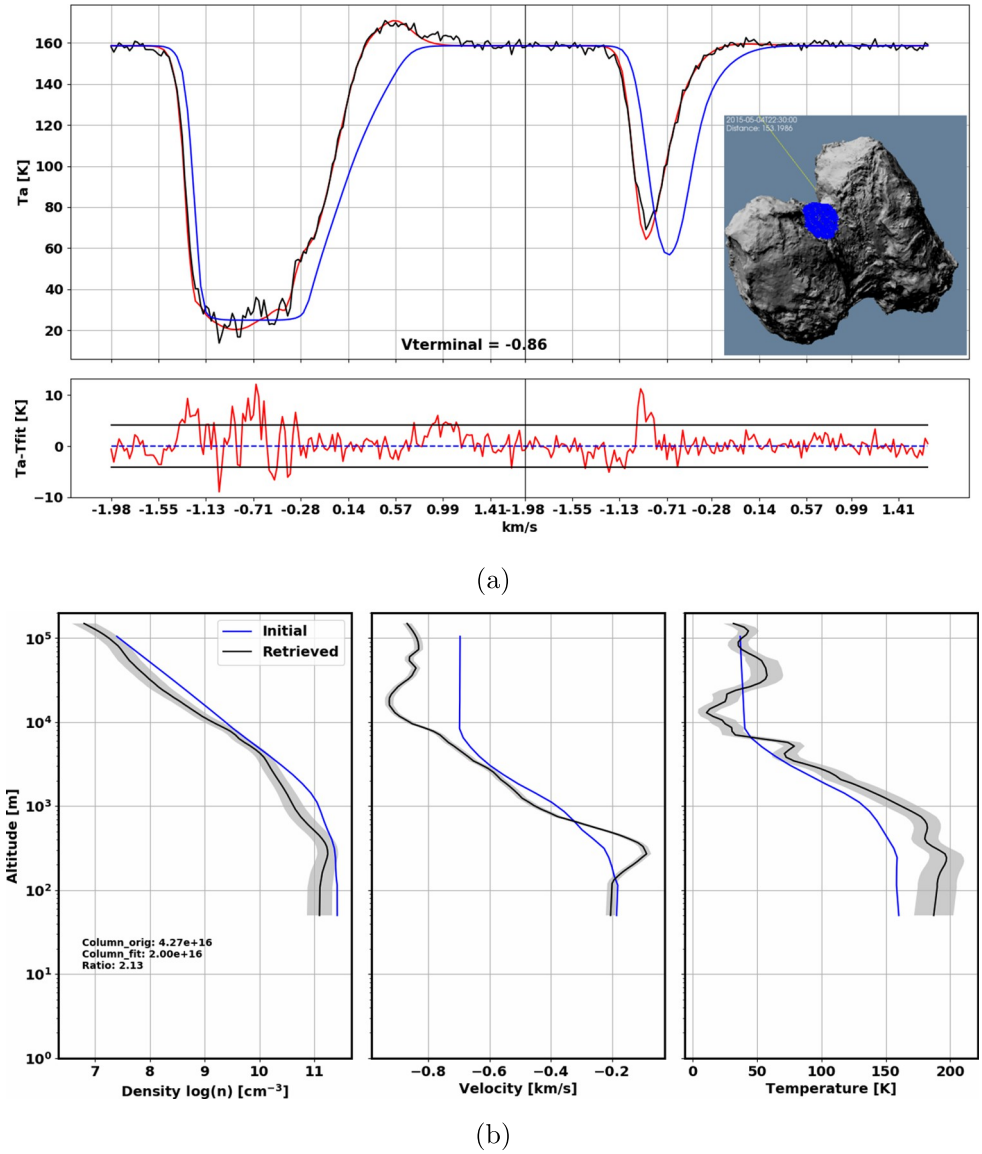

Fig. 15. Spectral lines and retrieved profiles for *case B*. The figure panels and colours have the same meaning as discussed in detail for *case A*. (a) Three spectra for the 557 GHz transitions of $H_2^{16}O$ (left) and $H_2^{18}O$ (right). (b) Vertical profiles of (left) number density, (middle) expansion velocity, and (right) kinetic temperature.

can be considered as an average velocity above about 20 km (where there is a change of slope in the profile) is still larger than 0.8 km/ s. Even in this case, the T_k(z) profile cannot be constant above ~10 km, and there is still some amount of heating (~50 km) as shown by the inversion in the T_k(z) profile. We also note that the model density profile for the initial iteration is close to the retrieved solution.

A more complex viewing geometry is presented in *case C*, shown in Fig. 16. From the inset, Fig. 16a, we see how the beam sounds the small lobe, nearly at the terminator. However, a large part of the illuminated portion of the larger lobe is also visible, and it is reasonable to assume that gas released from some of these facets would intersect the MIRO LOS which is 150 km in extent. Hence, we consider this a "complex" viewing geometry, such that other parts of the nucleus not directly in the MIRO FOV may contribute gas into the LOS. Regarding spectral line shapes, there are no interesting features that have not been identified and discussed previously. We include this example in part because of the notably weak $H_2^{18}O$ line, and because of the large discrepancy between initial (model) input water density and the retrieved one, which is already visible in the model spectra (blue lines). The estimated water density altitude profile (Fig. 16b) resembles the modelled one (though offset) up to heights of about 40–50 km, where it starts to increase. The velocity profile above 40–50 km is nearly constant, but the gas temperature shows a significant inversion, increasing rapidly from 7 to 10 km. Then the T_k(z) remains warm up to ~50 km and then decreases again. As discussed in connection with Fig. 12 (and in detail with Fig. 14) this is not a retrieval artefact. Using a constant temperature profile starting at any height above 10 km will not yield a good fit to the measured MIRO spectra.

In the *case D* shown in Fig. 17, the viewing geometry is such that the MIRO beam is fully on the illuminated Imhotep region. In Fig. 17a we can see that the retrieved profiles yield again very well the observed MIRO line shapes. We can also identify a rather weak, but discernible "red emission wing". Both $H_2^{16}O$ and $H_2^{18}O$ line shapes are highly asymmetric, implying non-constant velocity and temperature profiles up to high altitudes. The T_a temperatures exceed 225 K. In this example the interesting result is the rapid expansion speed (v_{exp}(z) > 0.9 km/ s) reached at the upper altitudes (averaged in the upper 20 km of the profile); see Fig. 17b. As in other examples, the gas T_k(z) shows an inversion at high altitudes, this time peaking close to 60 km, and with a large excess in temperatures (about 50 K) compared to the trend just below the heated layer. It also appears that the water density changed its gradient, and it does not decrease with height as $1/r^2$ for heights

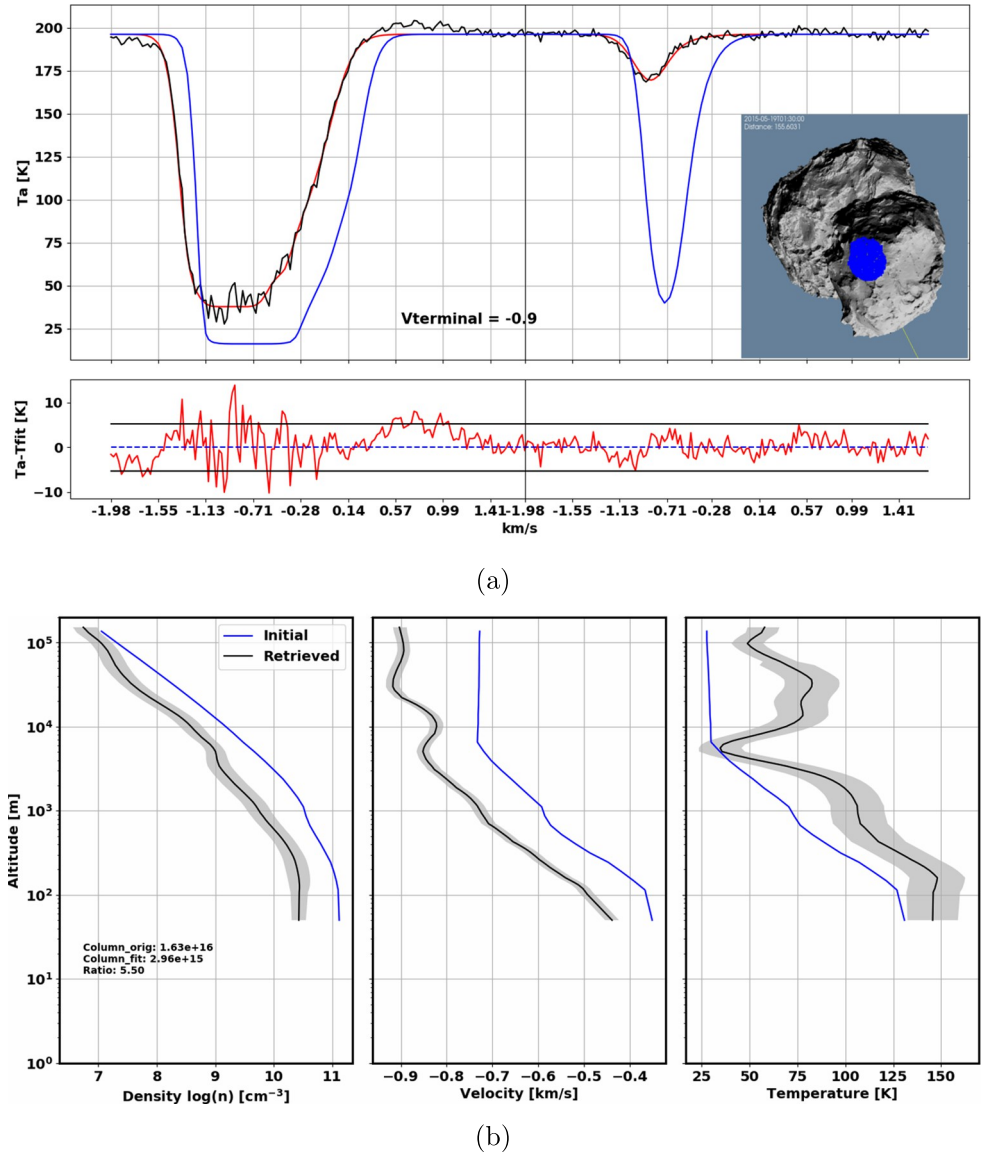

Fig. 16. Spectral lines and retrieved profiles for *case C*. The figure panels and colours have the same meaning as discussed in detail for *case A* (see Fig. 12). (a) Three spectra for the 557 GHz transitions of $H_2^{16}O$ (left) and $H_2^{18}O$ (right). (b) Vertical profiles of (left) number density, (middle) expansion velocity, and (right) kinetic temperature.

above 40 km.

At last we would like to draw attention to the fact that calibration of the MIRO spectrometer data is affected by up to 10% error in the knowledge of the side-band-ratio (SBR).[4] This bias cannot be precisely determined for both lines ($H_2^{16}O$ and $H_2^{18}O$), and it affects especially the line amplitude (while leaving the continuum temperature unaffected). We have investigated the role of this bias on our results separately by varying SBR through several values deviating from unity up to 15% for both lines simultaneously and re-running the retrievals. The largest effects is seen in temperature profiles for the upper altitudes (line core T_a is shifting with SBR changes, and most of the information on T_K is from the optically thick $H_2^{16}O$ line). The effects are such that the "warming" at altitudes around 40–50 km may be reduced up to 10–15 K for some cases, but enhanced for some other cases. However, on average the noted temperature enhancement at upper altitudes never disappears. This may be an indication that such feature does have presence in the real coma (although the absolute strength of this warming is poorly constrained right now by the MIRO data). A much stronger argument and perhaps physical explanation can be formed only after further thorough investigations, for example, the heliocentric dependence of this feature, whether it moves up/down with higher production rates, changes due to illumination, etc. We point this out, but nevertheless, such detailed work is beyond the scope of this paper.

4.4. OSIRIS comparisons

The dust distribution was computed for three example images from the wide angle camera (WAC) on OSIRIS from the sequence taken on 2018-05-05. A power-law size distribution for the dust was used, where the number of particles of a specific size, r, is proportional to r^{-b}. The power law index, b was chosen to be 2.5 which is slightly steeper than the recent paper by Merouane et al. (2016) would suggest from analysis of COSIMA and GIADA data. In all models we assume a constant dust-to-gas mass production rate ratio of 1.5 across the entire surface. We should mention that the dust-to-gas ratio is not independent of the size distribution. We have shown this dependency in Marschall et al.

4MIRO manual ftp://psa.esac.esa.int/pub/mirror/INTERNATIONAL-ROSETTA-MISSION/MIRO/RO-C-MIRO-4-EXT2-67P-V1.0/DOCUMENT/.

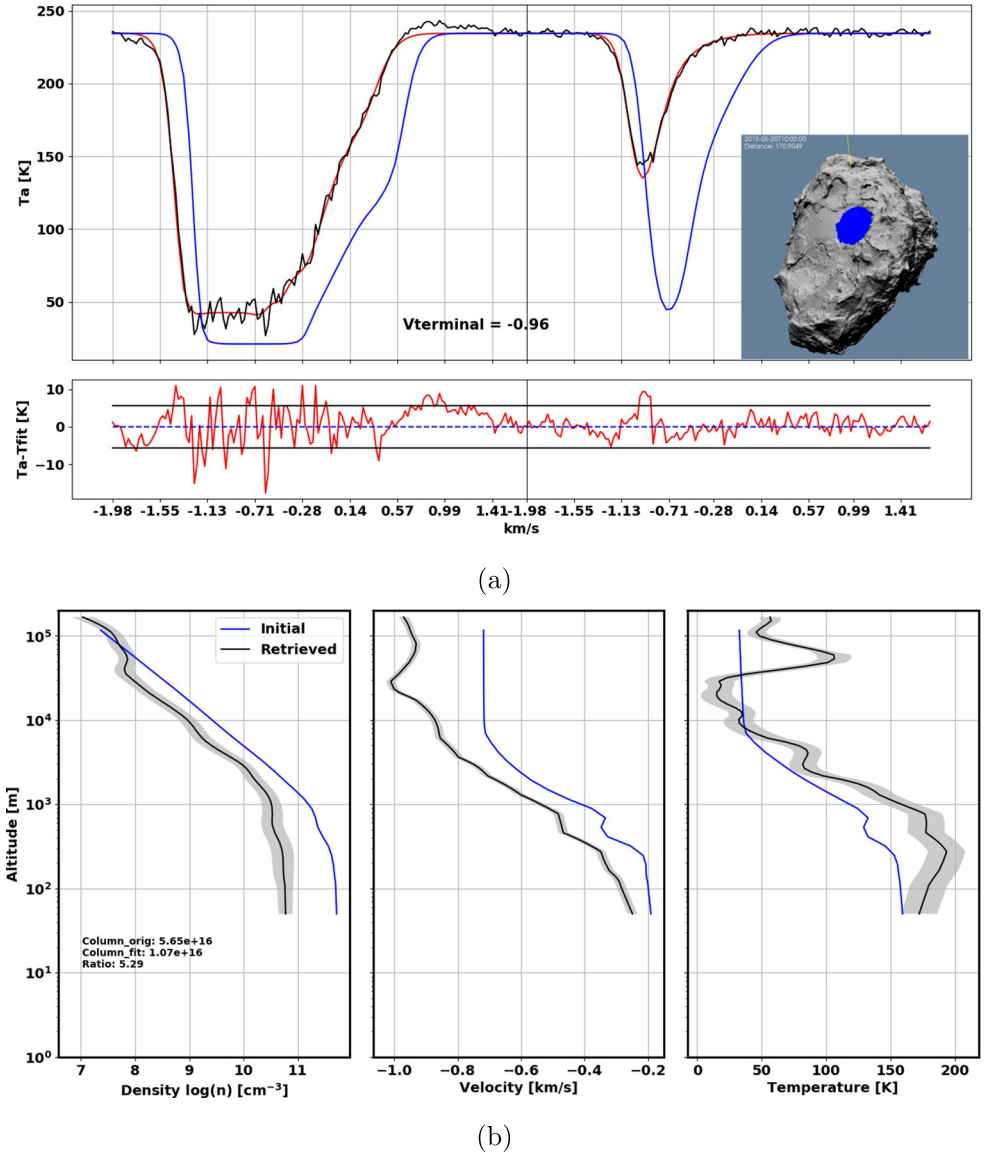

Fig. 17. Spectral lines and retrieved profiles for *case D*. The figure panels and colours have the same meaning as discussed in detail for *case A*. (a) Three spectra for the 557 GHz transitions of $H_2^{16}O$ (left) and $H_2^{18}O$ (right). (b) Vertical profiles of (left) number density, (middle) expansion velocity, and (right) kinetic temperature.

(Fig. 12 of 2016). A change in the dust size distribution will require a different dust-to-gas ratio to reproduce the same brightness as observed by OSIRIS.

For all three images in Figs. 18, 19, and 20 we show in the left panel the stretched and cropped OSIRIS-WAC image, in the centre panel the modelled dust brightness for the inhomogeneous model, and in the right panel the reflectance multiplied by the projected distance from the nucleus centre (impact parameter, d) as a function of azimuthal angle (AZ) on circle around the nucleus as indicated in the centre panel. The curves show the OSIRIS data (black line), the purely insolation-driven model (red line) and the inhomogeneous model (green line). The azimuthal plots allow us to see the details of the dust coma around the nucleus in a quantitative way. All images show the strong day (180°− 360° AZ) to night (0°− 180° AZ) variation of the dust brightness.

The three images in Figs. 18, 19, and 20 show that 1) an inhomogeneous gas emission distribution (inhomogeneous EAF) resulting in an inhomogeneous dust distribution in the coma is needed for a good first order fit, 2) slow moving particles originating from the Imhotep region can be seen, 3) variations in the illumination in combination with the local topography is sufficient for the production of most of the seen dust filaments in the second order fit, and 4) enhanced dust and/or gas emission from the Ma'at d) sub-region (Thomas et al., 2018) is needed. In general the regional inhomogeneous model fits the data very well. In the following we discuss these points in detail.

Firstly, Fig. 18 shows three large dust features on the day side at around 180°, 230°, and 315° AZ. Comparing these features it becomes clear that the inhomogeneous model (green line) does a much better job at reproducing the overall features than the purely insolation-driven model (red line). In particular the peak at 180° AZ is not reproduced well in the purely insolation-driven model. Additional dust emission is needed, the origin of which we could link to the sub-region Ma'at d) (Thomas et al., 2018). We will discuss this in more detail when looking at the third image which shows this effect more significantly. The interpretation of a χ^2 to determine the goodness of the fit can be challenging in this context because small peak shifts occur often and thus increase the χ^2 easily. We nevertheless calculate them to provide a metric of the goodness of the fit. For this image the χ^2 for the purely insolation driven model is 10.33 while it is 8.84 for the inhomogeneous model and thus the latter providing the better fit.

Secondly, when comparing the dust feature originating from Imhotep (producing the feature at about 315° AZ) in Fig. 18 the qualitative comparison between the OSIRIS image (left panel) and the simulation

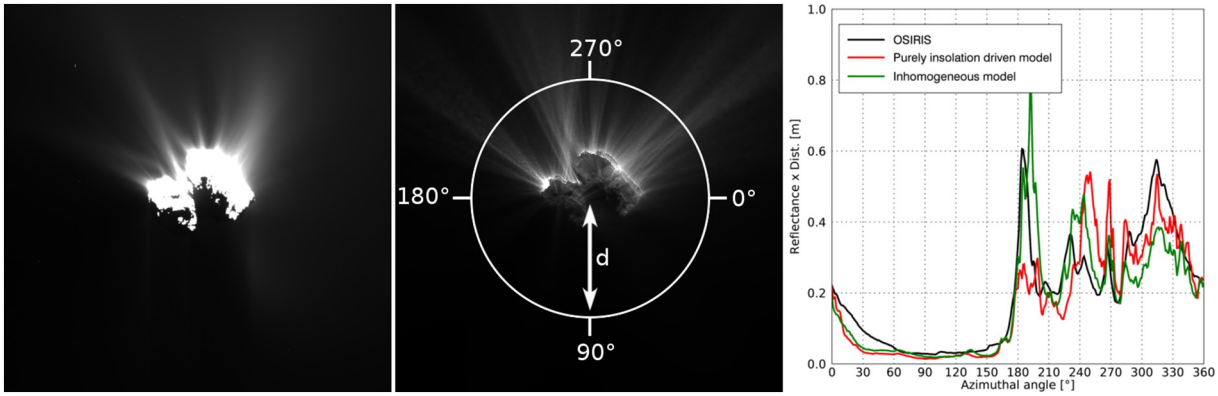

Fig. 18. Left panel: Stretched and cropped OSIRIS-WAC image taken on 2015-05-05 09:27:54 UTC. Centre panel: Modelled dust brightness for the inhomogeneous model. Right panel: Reflectance multiplied by the projected distance from the nucleus centre (impact parameter, d) as a function of azimuthal angle (AZ) on circle around the nucleus as indicated in the centre panel. The curves show the OSIRIS data (black line), the purely insolation-driven model (red line) and the inhomogeneous model (green line). Here $d = 2.5$ km.

(centre panel) shows that the feature in the OSIRIS image seems curved whereas the one in the simulation is straight. Two possible explanations for such features can be 1) optical illusion caused by crossing jets and this particular viewing geometry, or 2) slow moving (with respect to the nucleus rotation period) particles that result in a curved feature due to the Coriolis force. Regarding the former, we could not find sources that would produce such a curved feature. Other images in the sequence also show this curved feature from other viewing geometries. Furthermore Lin et al. (2016) and Shou et al. (2017) have possibly observed the same feature on 2015-05-30 OSIRIS data and found good fits with slow moving particles which further indicates the second explanation is likely the correct one. In Appendix A we model this feature and show the acceleration of the particles needed to fit the data. We find that between radial distances of 3 km and 5 km an average speed of 2.5 m s^{-1} is required whereas between 5 km and 10 km an average speed of 14 m s^{-1} is needed. We have employed a simple model including the comet rotation and gravity because our full model employed in this work is not time dependent. The details of this simpler model and its justification for this part of the analysis are outlined in Appendix A. These speeds are significantly higher than the ones found by Lin et al. (2016), but they are in general agreement with results by Shou et al. (2017). In contrast to Lin et al. (2016) we find that acceleration of the dust particles beyond 2 km from the surface is needed. This is in agreement with Gerig et al. (2018) who have found free radial outflow only after a distance of ~ 11 km from the nucleus which is also consistent with theoretical calculations by Zakharov et al. (2018).

Thirdly, in Fig. 19, we show a head-on view of Imhotep. Again the fit to the azimuthal plot is better for the inhomogeneous model although only slightly. As the EAF for the regions illuminated at this time does not vary very much, the gas coma is almost purely insolation-driven and does not have strong inhomogeneous features at the surface. Still this produces many dust filaments. Qualitatively many of these filaments are reproduced in our simulation. But these filaments are not produced by any local sources of gas but rather only by the variations of the illumination resulting in variations in the outgassing rate combined with the local topography which in some cases acts to focus features and in other cases makes them diffuse. This is very similar to the focusing first discussed by Keller et al. (1994) in the context of Giotto observations of filaments at comet Halley. For this image the χ^2 for the purely insolation driven model is 10.59 while it is 8.40 for the inhomogeneous model and thus the latter providing the better fit as with the previous image.

Fourthly, Fig. 20 shows the dust coma from a view with the comet's ‘ head’ with the Hatmehit region in the foreground. We have already mentioned a strong feature at 180° AZ in the OSIRIS image shown in Fig. 18. The dominant feature in the third image is this same dust filament seen a few hours later and is almost the only feature seen in the azimuthal plot at roughly 270° AZ. The purely insolation-driven model does not reproduce this feature in the necessary strength, and the inhomogeneous model is also quite uniform in EAF for the ‘ head’ of the comet (see Fig. 6). The feature seen in the green line in Fig. 20 can be the result of three different effects affecting the sub-region Ma’at d) which is shown in Fig. 21: Either the local dust-to-gas mass production rate ratio of the sub-region Ma’at d) must be a factor of 8 higher than anywhere else on the comet (to this point we have always assumed a constant dust-to-gas mass production rate ratio) or the EAF for the gas of the sub-region Ma’at d) must be a factor 36 higher than in the inhomogeneous model. A further possibility would be a different emitted

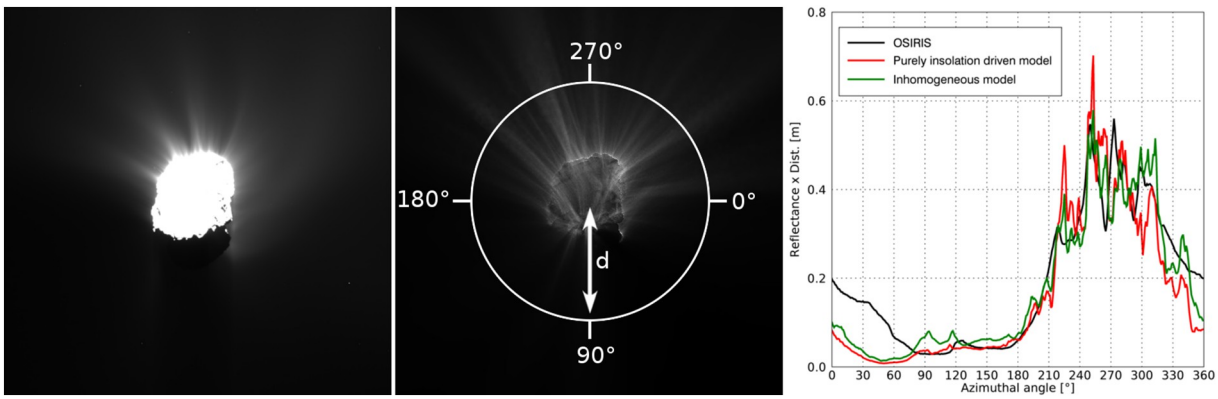

Fig. 19. Left panel: Stretched and cropped OSIRIS-WAC image taken on 2015-05-05 06:28:54 UTC. Centre and right panel analogous to Fig. 18. Here $d = 3.0$ km.

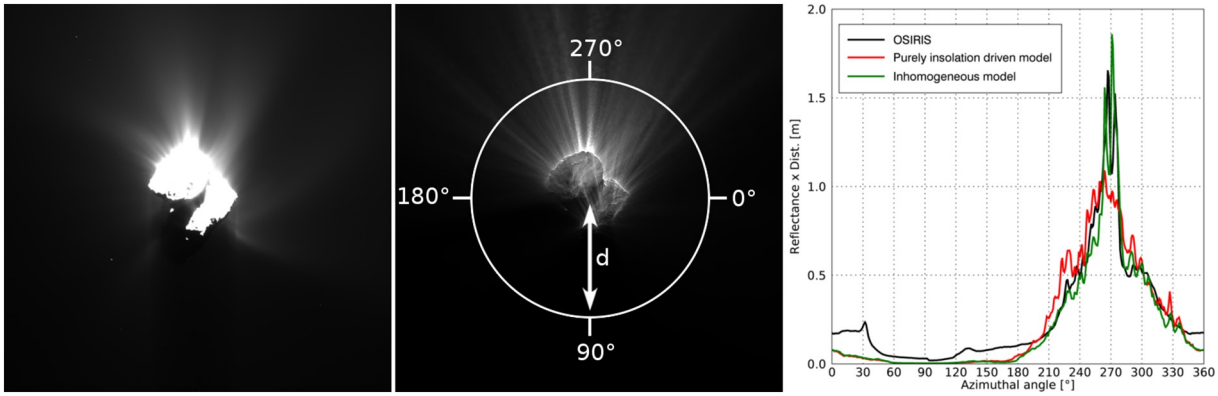

Fig. 20. Left panel: Stretched and cropped OSIRIS-WAC image taken on 2015-05-05 12:27:54 UTC. Centre and right panel analogous to Fig. 19. Here $d = 2.5$ km.

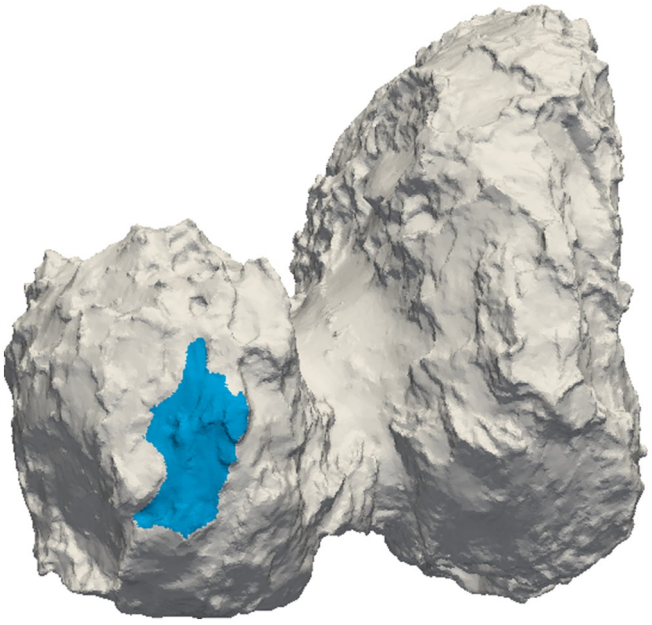

Fig. 21. View of the shape model highlighting the region Ma'at d) (Thomas et al., 2018) in blue which shows enhanced dust emission during the studied epoch as seen in Fig. 20.

dust size distribution dominated by more optically active particles than on the rest of the comet. In all other cases we have assumed the same power law dust size distribution with power law exponent of − 2.5 across the entire surface. Any of these effects, single or in combination, can account for this prominent dust feature, which clearly calls for further investigation as this sub-region seems to be "special". For this final image the χ^2 for the purely insolation driven model is 15.36 while it is 13.73 for the inhomogeneous model. As for the other two images the inhomogeneous model provides the better fit.

Finally, we have seen that in all presented cases the regionally inhomogeneous model reproduces the data to a high degree including even many small filaments. We have also highlighted several different ways with which dust filaments are reproduced in our model (e.g. due to inhomogeneous gas emission or topographic focusing).

5. Conclusions

We have built a comprehensive modelling pipeline that allows a self-consistent description of the inner gas and dust comae providing output for direct comparison with all major instruments on-board Rosetta that studied the inner coma. We have iteratively tuned model parameters to reproduce ROSINA, VIRTIS, MIRO, and OSIRIS data acquired in the May 2015 time-frame. We have compared the data to two models - a purely insolation-driven and a regionally inhomogeneous one - shown in Fig. 6. These two models are the start and end points of our iterative process. We begin with the purely insolation driven model as a benchmark model with the least number of free parameters. Then the EAF of different regions are varied and the results tested against the different data sets. Different instruments are often sensitive to different changes, and hence different measurements confirm or rule out certain assumptions of the EAF. The regionally inhomogeneous models represented the best fit found. We will summarise the conclusions we can draw from the comparison with each individual instrument in separate sections. But first, we will summarise which model explains the respective data set better. We also summarise in Table 2 the values we found to compare which model fits the data better and thus supports the following conclusions.

- **ROSINA:** The models perform almost equally well. There is only a slightly better fit of the inhomogeneous model with measured data but in this case ROSINA does not provide a strong constraint during this period.
- **VIRTIS:** We have seen good agreement of the inhomogeneous model with the data which is not the case for the purely insolation driven model.
- **MIRO:** We have seen a good qualitative agreement of the inhomogeneous model with the data - higher emission from the ' Neck' and lower emission from elsewhere, especially the Imhotep region. A detailed summary from the inversion for line-of-sight (LOS) profiles is given below.
- **OSIRIS:** We have seen good agreement of the inhomogeneous model with the data. The purely insolation-driven model does not reproduce the data.

Table 2
Summary of the mean difference, Δ, and χ^2 of the two models with regards to the measurements of the different instruments.

	ROSINA (Δ)[III]	VIRTIS (χ^2)[IV]		OSIRIS (χ^2)[II]		
		Cube a)	Cube g)	Fig. 18	Fig. 19	Fig. 20
insol.[I]	33.6%	47.9	20.6	10.33	10.59	15.36
inhom.[II]	27.6%	7.61	8.70	8.84	8.40	13.73

Notes.
[I] Purely insolation-driven model.
[II] Regionally inhomogeneous model.
[III] $\Delta = \frac{1}{N}\Sigma_{i=1}^{N}\frac{x_i - m_i}{m_i}$, where N, is the number of measurements, x_i is the model value, and m_i is the respective measured value.
[IV] $\chi^2 = \Sigma_{i=1}^{N}\frac{(x_i - m_i)^2}{m_i}$. For MIRO we refer to Section 4.3 which provides a detailed discussion of the fits.

Although the fact that the source distribution is non-uniform has been shown in other studies (e.g. Marschall et al., 2016; Fougere et al., 2016; Zakharov et al., 2018) this study shows a good agreement of our model across data from four Rosetta instruments. As far as we are aware this is novel. The modelling pipeline presented here demonstrates how measurements from multiple Rosetta instruments can be simulated within one consistent framework. The comparison between the instruments has shown foremost the need for a multi-instrument approach to determine which model assumptions provides better agreement with Rosetta data sets as a whole when a single instrument is not able to do so. The one missing piece to date is the fact that there is no model of the surface that explains cometary activity from first principles. This should be the focus of future work of the community.

5.1. Sensitivity of the model to ROSINA data

We use ROSINA/COPS data as the initial constraint for models of the inner gas coma. We have previously shown in Marschall et al. (2017) that very different model assumptions on the surface outgassing distribution can lead to statistically equally good fits to the ROSINA/COPS data. This shows the limitations of the single-instrument approach - in this case ROSINA/COPS - to determine accurately the emission distribution at the surface of the comet. In particular, variations in the gas distribution close to the surface were difficult to distinguish for reasons that have been addressed in part by other authors (e.g. Liao et al., 2018). Importantly, this demonstrates that a multi-instrument approach is essential in constraining the innermost part of the coma. For the equinox (May 2015) observations discussed here, a similar picture has emerged. Insolation-driven and inhomogeneous models were even more difficult to differentiate in this case although the inhomogeneous model used here seems to provide better fits. In particular, the Imhotep and Hatmehit regions of the nucleus showed low gas emission as would have been predicted from the November 2014 results. The reduced sensitivity to the emission distribution may result from the higher cometocentric distance of the spacecraft at equinox ($\sim$ 150–200 km) and collisions more rapidly washing out gas structures originating from the non-uniform outgassing properties on the surface and the comet's irregular shape.

5.2. VIRTIS summary

We have presented results comparing VIRTIS-M-IR cubes analysed in Migliorini et al. (2016) with our model predictions. The VIRTIS data provide an unambiguous constraint that leads to a clear preference for the inhomogeneous model. In particular, as Migliorini et al. (2016) noted, the emission from Imhotep is very weak. The gas column density over Imhotep when it is illuminated is massively over-predicted when assuming purely insolation-driven outgassing over the entire surface. This fits well the interpretation of the November 2014 data by Marschall et al. (2016) that activity on Imhotep is lower than elsewhere on the nucleus. This might be somewhat surprising given the significant surface changes seen in Imhotep over the mission (El-Maarry et al., 2016). The higher emission of H_2O from the “Neck” regions (Hapi) also appears to be confirmed by comparison with the VIRTIS-M data. These data provide an important additional constraint on the emission and thus the inhomogeneities of the surface.

5.3. MIRO summary

The MIRO instrument allows for a LOS analysis through the inner gas coma and thus has the potential to constrain smaller scale variations of the surface gas emission distribution compared to instruments such as ROSINA or VIRTIS. Relying on the measured $H_2^{16}O$ and $H_2^{18}O$ line shapes we are now able to reconstruct the LOS altitude profile of H_2O number density, velocity, and temperature in nadir geometry. This gives unprecedented information on the structure of the gas coma with high accuracy down to 100 m above the surface. Performing this retrieval for 71 observations around equinox in May 2015 we were able to derive the following main points and conclusions.

- The MIRO spectra imply a significantly smaller water density profile than the 3D model, and this is also true for the column density. The retrieved altitude profile shows that water is consistent with the $1/r^2$ dependence, except for the density profile in the high altitude region 50–60 km, where the density slope changes (slower decay).
- During the period under study, the MIRO observations of the “Neck” region always yield a higher water column density compared to other regions of similar illumination. The overall variability of all retrieved MIRO column densities varies from about 2×10^{15} to 3×10^{16} molecules cm^{-2}. However, even terminator or non-illuminated areas within the FOV show considerable density. Therefore, even MIRO observations with a relatively small FOV cannot determine active versus inactive surfaces. This result is perhaps somewhat unexpected.
- The retrieved LOS expansion velocity implies that gas is accelerating most of the time well above 10–20 km altitude, and relative to the modelled profiles the gas seems to be faster by about 50–100 m/s.
- Similarly, the retrieved gas kinetic temperature is warmer than the model predicted by 20–40 K on average.
- The temperature profiles show a persistent warming feature in the high altitudes, around 40–50 km. Taking into account the behaviour of the density (slower fall-off), and the bulk velocity (also showing slow-down) we tentatively postulate that local sublimation from lifted dust/ice particles may be consistent with this feature. This hypothesis is attractive, because the warm region in the upper atmosphere is prevalent even over the terminator or for poorly illuminated coma conditions. Perhaps, the water ice particles are lifted by the more volatile gases which MIRO cannot detect, such as CO_2 or CO. However, there are other factors that need to be investigated in more detail before settling this issue, namely the role of electrons in the water molecule excitation. We have made a preliminary study for few cases of electron densities and temperatures, however, even for optimistic values a maximum heating of 10 K was obtained, which is still not enough for the 20–30 K warming shown in the temperature profile.
- Another persistent and directly observed feature is the “red emission wing” in the $H_2^{16}O$ line shape. We do not attempt to fit this spectral region by penalizing the retrieval routine, however, we discuss that it would imply a very low gas speed and high temperature at lower altitude (0–400 m), almost a “stagnant” layer of gas around the nucleus. Again, we leave the resolution of this issue to a later investigation.
- The approach of using 3D model profiles as the starting conditions for the MIRO retrieval proved extremely useful. The 3D model is able to provide physics-based profiles, which are much better than the typical approach of using the Haser model (Haser, 1957) for density, empirical velocity and temperature profiles. It allowed us to fit the complex line shapes of MIRO spectra to within 2σ of the measured random noise.

5.4. OSIRIS summary

We have seen that some of our conclusions from the analysis of measurements by other instruments are supported by the synthetic OSIRIS images of the dust emission. In particular, we have shown that an inhomogeneous gas emission caused by a regionally inhomogeneous EAF distribution in conjunction with illumination variations results in the inhomogeneous dust distribution in the coma needed for a good fit to the data. Additionally we have seen slow-moving particles originating from the Imhotep region. Their average speed between 3 and 10 km distance from the nucleus centre of mass is 8 m s^{-1} but we have also seen the effect of dust acceleration due to the gas drag as the

average speed between 3 and 5 km is 2.5 m s^{-1} but 14 m s^{-1} between 5 and 10 km. We have also demonstrated that variations in the illumination in combination with the local topography is sufficient for the production of most of the seen smaller dust filaments. Furthermore we could determine an enhanced dust and/or gas emission from the Ma'at d) sub-region.

Acknowledgements

The team from the University of Bern is supported through the Swiss National Science Foundation and through the NCCR PlanetS. The project has also received funding from the European Union's Horizon 2020 research and innovation programme under grant agreement no 686709. This work was supported by the Swiss State Secretariat for Education, Research and Innovation (SERI) under contract number 16.0008-2. The opinions expressed and arguments employed herein do not necessarily reflect the official views of the Swiss Government. A part of this research was carried out at the Max-Planck-Institute für Sonnensystemforschung with financial support from Deutsche Forschungsgemeinschaft (DFG), Germany and the Max Planck Gesellschaft within the IMPRS programme. We acknowledge personnel at ESA's European Space Operations Center (ESOC) in Darmstadt, Germany, European Space Astronomy Center (ESAC) in Spain, and at ESA, and NASA/JPL for the making the Rosetta mission possible.

Appendix A. Slow moving dust particles

In this appendix we model the curved dust feature originating from Imhotep as seen in Fig. 18. In the image the dust peak azimuth moved by -11.2° AZ from a distance of $d = 3$ km to $d = 5$ km and an additional -5.9° AZ from a distance of $d = 5$ km to $d = 10$ km. We have therefore run a gravitational model to determine the dust speed that would reproduce this kind of shift. Particles are launched with a certain initial speed from the surface of Imhotep and are then tracked through the gravity field taking into account the effect of the rotating nucleus. The Imhotep region was illuminated for approximately 4 h prior to the acquisition of the OSIRIS image of Fig. 18. Hence we assume this is the maximum time prior to which particles could have been emitted and thus this is the duration for which the simulation was run. Fig. A.22 shows the results for three different initial dust speeds (2.5 m s^{-1}, 8 m s^{-1}, and 14 m s^{-1}) for these simulations as column density plots as well as azimuthal plots to measure the angular motion of the dust feature. The qualitative assessment of the curvatures seen in the top panels of Fig. A.22 shows differences, but it is difficult to match the simulation to the data, so a quantitative perspective is needed. Table A.3 gives the angular difference of the Imhotep peaks between two impact parameters. We see that even though the dust-gas interaction and thus acceleration is not taken into account, the results still give us information about the change in particle speeds. The simulation with an initial speed of 8 m s^{-1} gives the best fit to the total displacement between 3 km–10 km. It is thus reasonable to assume that this feature is dominated by particles moving at an average speed of 8 m s^{-1}. But going into more detail we see that between 3 km–5 km the average dust speed needs to be 2.5 m s^{-1} and between 5 km and 10 km the average dust speed matching best is 14 m s^{-1}. This shows the acceleration of the particles driven by the gas flow. These simulations do not depend on the particle mass or size. Therefore it is not possible to uniquely determine the dust size from this analysis alone. Only by linking this result with our dust dynamics simulation including gas drag can we estimate the dust size. It is important to state here that this estimate of the dust size is degenerate with regard to the size and mass of the particles. A large particle with low density will behave similarly as a small particle with a high density.

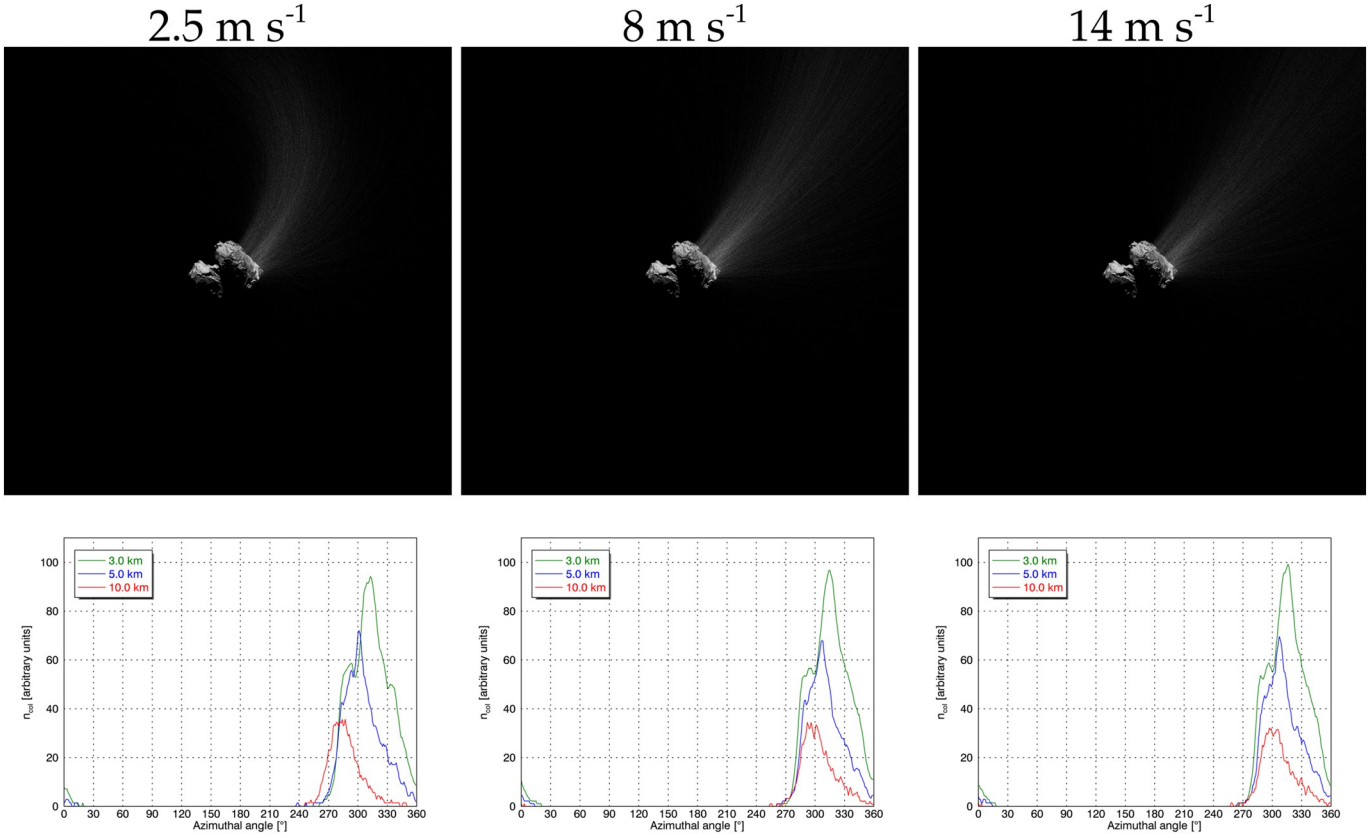

Fig. A.22. The top row shows the dust column density, $n_c ol$, for three different initial speeds (2.5 m s^{-1}, 8 m s^{-1}, and 14 m s^{-1}) of dust particles originating from the Imhotep region. The viewing geometry was chosen to be the one of the OSIRIS image of Fig. 18. The bottom row shows for each of the initial dust speeds the column density as a function of the azimuthal angle as in the right panel of Fig. 18.

Table A.3
Change in azimuth, $\Delta\phi$, of the Imhotep peak between two impact parameters, d, measured in the azimuthal plots of Fig. A.22. Marked in bold are the values resembling closest the OSIRIS values.

$\Delta\phi$	OSIRIS	2.5 m s^{-1}	8 m s^{-1}	14 m s^{-1}
3 km–5 km	− 11.2°	**− 11.1°**	− 7.6°	− 7.5°
5 km–10 km	− 5.9°	− 19.2°	− 9.5°	**− 5.8°**
3 km–10 km	− 17.1°	− 30.3°	**− 17.0°**	− 13.4°

References

Acton, C.H., 1996, Jan, Jan. Ancillary data services of NASA's navigation and ancillary information facility. Planet. Space Sci. 44, 65–70. https://doi.org/10.1016/0032-0633(95)00107-7.

Balsiger, H., Altwegg, K., Bochsler, P., Eberhardt, P., Fischer, J., Graf, S., Jäckel, A., Kopp, E., Langer, U., Mildner, M., Müller, J., Riesen, T., Rubin, M., Scherer, S., Wurz, P., Wüthrich, S., Arijs, E., Delanoye, S., de Keyser, J., Neefs, E., Nevejans, D., Rème, H., Aoustin, C., Mazelle, C., Médale, J.-L., Sauvaud, J.A., Berthelier, J.-J., Bertaux, J.-L., Duvet, L., Illiano, J.M., Fuselier, S.A., Ghielmetti, A.G., Magoncelli, T., Shelley, E.G., Korth, A., Heerlein, K., Lauche, H., Livi, S., Loose, A., Mall, U., Wilken, B., Gliem, F., Fiethe, B., Gombosi, T.I., Block, B., Carignan, G.R., Fisk, L.A., Waite, J.H., Young, D.T., Wollnik, H., 2007. Rosina Rosetta orbiter spectrometer for ion and neutral analysis. Space Sci. Rev. 128, 745–801. https://doi.org/10.1007/s11214-006-8335-3.

Bertini, I., La Forgia, F., Tubiana, C., Güttler, C., Fulle, M., Moreno, F., Frattin, E., Kovacs, G., Pajola, M., Sierks, H., Barbieri, C., Lamy, P., Rodrigo, R., Koschny, D., Rickman, H., Keller, H.U., Agarwal, J., A'Hearn, M.F., Barucci, M.A., Bertaux, J.L., Bodewits, D., Cremonese, G., Da Deppo, V., Davidsson, B., Debei, S., De Cecco, M., Drolshagen, E., Ferrari, S., Ferri, F., Fornasier, S., Gicquel, A., Groussin, O., Gutierrez, P.J., Hasselmann, P.H., Hviid, S.F., Ip, W.H., Jorda, L., Knollenberg, J., Kramm, J.R., Kuührt, E., Kuüppers, M., Lara, L.M., Lazzarin, M., Lin, Z.Y., Moreno, J.J.L., Lucchetti, A., Marzari, F., Massironi, M., Mottola, S., Naletto, G., Oklay, N., Ott, T., Penasa, L., Thomas, N., Vincent, J.B., 2017. The scattering phase function of comet 67P/Churyumov-Gerasimenko coma as seen from the Rosetta/OSIRIS instrument. MNRAS 469, S404–S415. https://doi.org/10.1093/mnras/stx1850.

Bieler, A., Altwegg, K., Balsiger, H., Berthelier, J.-J., Calmonte, U., Combi, M., De Keyser, J., Fiethe, B., Fougere, N., Fuselier, S., Gasc, S., Gombosi, T., Hansen, K., Hässig, M., Huang, Z., Jäckel, A., Jia, X., Le Roy, L., Mall, U.A., Rème, H., Rubin, M., Tenishev, V., Tóth, G., Tzou, C.-Y., Wurz, P., 2015. Comparison of 3D kinetic and hydrodynamic models to ROSINA-COPS measurements of the neutral coma of 67P/Churyumov-Gerasimenko. Astron. Astrophys. 583, A7. https://doi.org/10.1051/0004-6361/201526178.

Biver, N., Hofstadter, M., Gulkis, S., Bockelée-Morvan, D., Choukroun, M., Lellouch, E., Schloerb, F.P., Rezac, L., Ip, W.H., Jarchow, C., Hartogh, P., Lee, S., von Allmen, P., Crovisier, J., Leyrat, C., Encrenaz, P., 2015. Distribution of water around the nucleus of comet 67P/Churyumov-Gerasimenko at 3.4 AU from the Sun as seen by the MIRO instrument on Rosetta. Astron. Astrophys. 583, A3. https://doi.org/10.1051/0004-6361/201526094.

Bockelée-Morvan, D., Debout, V., Erard, S., Leyrat, C., Capaccioni, F., Filacchione, G., Fougere, N., Drossart, P., Arnold, G., Combi, M., Schmitt, B., Crovisier, J., de Sanctis, M.-C., Encrenaz, T., Kührt, E., Palomba, E., Taylor, F.W., Tosi, F., Piccioni, G., Fink, U., Tozzi, G., Barucci, A., Biver, N., Capria, M.-T., Combes, M., Ip, W., Blecka, M., Henry, F., Jacquinod, S., Reess, J.-M., Semery, A., Tiphene, D., 2015. First observations of H_2O and CO_2 vapor in comet 67P/Churyumov-Gerasimenko made by VIRTIS onboard Rosetta. Astron. Astrophys. 583, A6. https://doi.org/10.1051/0004-6361/201526303.

Bohren, C.F., Huffman, D.R., 1983. Absorption and Scattering of Light by Small Particles.

Choukroun, M., Keihm, S., Schloerb, F.P., Gulkis, S., Lellouch, E., Leyrat, C., von Allmen, P., Biver, N., Bockelée-Morvan, D., Crovisier, J., Encrenaz, P., Hartogh, P., Hofstadter, M., Ip, W.-H., Jarchow, C., Janssen, M., Lee, S., Rezac, L., Beaudin, G., Gaskell, B., Jorda, L., Keller, H.U., Sierks, H., 2015. Dark side of comet 67P/Churyumov-Gerasimenko in Aug.-Oct. 2014. MIRO/Rosetta continuum observations of polar night in the southern regions. Astron. Astrophys. 583, A28. https://doi.org/10.1051/0004-6361/201526181.

Christou, C., Dadzie, S.K., Thomas, N., Marschall, R., Hartogh, P., Jorda, L., Kührt, E., Wright, I., Rodrigo, R., 2018. Gas flow in near surface comet like porous structures: application to 67P/Churyumov-Gerasimenko. Planet. Space Sci. 161, 57–67. https://doi.org/10.1016/j.pss.2018.06.009.

Coradini, A., Capaccioni, F., Drossart, P., Arnold, G., Ammannito, E., Angrilli, F., Barucci, A., Bellucci, G., Benkhoff, J., Bianchini, G., Bibring, J.P., Blecka, M., Bockelee-Morvan, D., Capria, M.T., Carlson, R., Carsenty, U., Cerroni, P., Colangeli, L., Combes, M., Combi, M., Crovisier, J., De Sanctis, M.C., Encrenaz, E.T., Erard, S., Federico, C., Filacchione, G., Fink, U., Fonti, S., Formisano, V., Ip, W.H., Jaumann, R., Kuehrt, E., Langevin, Y., Magni, G., McCord, T., Mennella, V., Mottola, S., Neukum, G., Palumbo, P., Piccioni, G., Rauer, H., Saggin, B., Schmitt, B., Tiphene, D., Tozzi, G., 2007. Virtis: an imaging spectrometer for the Rosetta Mission. Space Sci. Rev. 128, 529–559. https://doi.org/10.1007/s11214-006-9127-5.

Davidsson, B.J.R., Sierks, H., Güttler, C., Marzari, F., Pajola, M., Rickman, H., A'Hearn, M.F., Auger, A.T., El-Maarry, M.R., Fornasier, S., Gutiérrez, P.J., Keller, H.U., Massironi, M., Snodgrass, C., Vincent, J.B., Barbieri, C., Lamy, P.L., Rodrigo, R., Koschny, D., Barucci, M.A., Bertaux, J.L., Bertini, I., Cremonese, G., Da Deppo, V., Debei, S., De Cecco, M., Feller, C., Fulle, M., Groussin, O., Hviid, S.F., Hoöfner, S., Ip, W.H., Jorda, L., Knollenberg, J., Kovacs, G., Kramm, J.R., Kührt, E., Küppers, M., La Forgia, F., Lara, L.M., Lazzarin, M., Lopez Moreno, J.J., Moissl-Fraund, R., Mottola, S., Naletto, G., Oklay, N., Thomas, N., Tubiana, C., 2016. The primordial nucleus of comet 67P/Churyumov-Gerasimenko. Astron. Astrophys. 592, A63. https://doi.org/10.1051/0004-6361/201526968.

Debout, V., Bockelée-Morvan, D., Zakharov, V., 2016, Feb, Feb. A radiative transfer model to treat infrared molecular excitation in cometary atmospheres. Icarus 265, 110–124. https://doi.org/10.1016/j.icarus.2015.10.013.

El-Maarry, M.R., Thomas, N., Gracia-Berná, A., Pajola, M., Lee, J.C., Massironi, M., Davidsson, B., Marchi, S., Keller, H.U., Hviid, S.F., Besse, S., Sierks, H., Barbieri, C., Lamy, P.L., Koschny, D., Rickman, H., Rodrigo, R., A'Hearn, M.F., Auger, A.T., Barucci, M.A., Bertaux, J.L., Bertini, I., Bodewits, D., Cremonese, G., Da Deppo, V., De Cecco, M., Debei, S., Güttler, C., Fornasier, S., Fulle, M., Giacomini, L., Groussin, O., Gutierrez, P.J., Ip, W.H., Jorda, L., Knollenberg, J., Kovacs, G., Kramm, J.R., Kührt, E., Küppers, M., Lara, L.M., Lazzarin, M., Lopez Moreno, J.J., Marschall, R., Marzari, F., Naletto, G., Oklay, N., Pommerol, A., Preusker, F., Scholten, F., Tubiana, C., Vincent, J.B., 2016. Regional surface morphology of comet 67P/Churyumov-Gerasimenko from Rosetta/OSIRIS images: the southern hemisphere. Astron. Astrophys. 593, A110. https://doi.org/10.1051/0004-6361/201628634.

Eriksson, P., 2000, Jul, Jul. Analysis and comparison of two linear regularization methods for passive atmospheric observations. J. Geophys. Res. 105, 18. https://doi.org/10.1029/2000JD900172.

Fornasier, S., Feller, C., Lee, J.C., Ferrari, S., Massironi, M., Hasselmann, P.H., Deshapriya, J.D.P., Barucci, M.A., El-Maarry, M.R., Giacomini, L., Mottola, S., Keller, H.U., Ip, W.H., Lin, Z.Y., Sierks, H., Barbieri, C., Lamy, P.L., Rodrigo, R., Koschny, D., Rickman, H., Agarwal, J., A'Hearn, M., Bertaux, J.L., Bertini, I., Cremonese, G., Da Deppo, V., Davidsson, B., Debei, S., De Cecco, M., Deller, J., Fulle, M., Groussin, O., Gutierrez, P.J., Güttler, C., Hofmann, M., Hviid, S.F., Jorda, L., Knollenberg, J., Kovacs, G., Kramm, R., Kührt, E., Küppers, M., Lara, M.L., Lazzarin, M., Lopez Moreno, J.J., Marzari, F., Naletto, G., Oklay, N., Pajola, M., Shi, X., Thomas, N., Toth, I., Tubiana, C., Vincent, J.B., 2017. The highly active Anhur-Bes regions in the 67P/Churyumov-Gerasimenko comet: results from OSIRIS/ROSETTA observations. MNRAS 469, S93–S107. https://doi.org/10.1093/mnras/stx1275.

Fornasier, S., Hasselmann, P.H., Barucci, M.A., Feller, C., Besse, S., Leyrat, C., Lara, L., Gutierrez, P.J., Oklay, N., Tubiana, C., Scholten, F., Sierks, H., Barbieri, C., Lamy, P.L., Rodrigo, R., Koschny, D., Rickman, H., Keller, H.U., Agarwal, J., A'Hearn, M.F., Bertaux, J.-L., Bertini, I., Cremonese, G., Da Deppo, V., Davidsson, B., Debei, S., De Cecco, M., Fulle, M., Groussin, O., Güttler, C., Hviid, S.F., Ip, W., Jorda, L., Knollenberg, J., Kovacs, G., Kramm, R., Kührt, E., Küppers, M., La Forgia, F., Lazzarin, M., Lopez Moreno, J.J., Marzari, F., Matz, K.D., Michalik, H., Moreno, F., Mottola, S., Naletto, G., Pajola, M., Pommerol, A., Preusker, F., Shi, X., Snodgrass, C., Thomas, N., Vincent, J.B., 2015. Spectrophotometric properties of the nucleus of comet 67P/Churyumov-Gerasimenko from the OSIRIS instrument onboard the ROSETTA spacecraft. ArXiv e-prints. arXiv:1505.06888.

Fougere, N., Altwegg, K., Berthelier, J.J., Bieler, A., Bockelée-Morvan, D., Calmonte, U., Capaccioni, F., Combi, M.R., De Keyser, J., Debout, V., Erard, S., Fiethe, B., Filacchione, G., Fink, U., Fuselier, S.A., Gombosi, T.I., Hansen, K.C., Hässig, M., Huang, Z., Le Roy, L., Leyrat, C., Migliorini, A., Piccioni, G., Rinaldi, G., Rubin, M., Shou, Y., Tenishev, V., Toth, G., Tzou, C.Y., 2016. Three-dimensional direct simulation Monte-Carlo modeling of the coma of comet 67P/Churyumov-Gerasimenko observed by the VIRTIS and ROSINA instruments on board Rosetta. Astron. Astrophys. 588, A134. https://doi.org/10.1051/0004-6361/201527889.

Gasc, S., Altwegg, K., Balsiger, H., Berthelier, J.-J., Bieler, A., Calmonte, U., Fiethe, B., Fuselier, S., Galli, A., Gombosi, T., Hoang, M., De Keyser, J., Korth, A., Le Roy, L., Mall, U., Rème, H., Rubin, M., Sémon, T., Tzou, C.-Y., Waite, J.H., Wurz, P., 2017. Change of outgassing pattern of 67P/Churyumov-Gerasimenko during the March 2016 equinox as seen by ROSINA. MNRAS 469, S108–S117. https://doi.org/10.1093/mnras/stx1412.

Gerig, S.B., Marschall, R., Thomas, N., Bertini, I., Bodewits, D., Davidsson, B., Fulle, M., Ip, W.H., Keller, H.U., Küppers, M., Preusker, F., Scholten, F., Su, C.C., Toth, I., Tubiana, C., Wu, J.S., Sierks, H., Barbieri, C., Lamy, P.L., Rodrigo, R., Koschny, D., Rickman, H., Agarwal, J., Barucci, M.A., Bertaux, J.L., Cremonese, G., Da Deppo, V., Debei, S., De Cecco, M., Deller, J., Fornasier, S., Groussin, O., Gutierrez, P.J., Güttler, C., Hviid, S.F., Jorda, L., Knollenberg, J., Kramm, J.R., Kührt, E., Lara, L.M., Lazzarin, M., Lopez Moreno, J.J., Marzari, F., Mottola, S., Naletto, G., Oklay, N., Vincent, J.B., 2018. On deviations from free-radial outflow in the inner coma of comet 67P/Churyumov-Gerasimenko. Icarus 311, 1–22. https://doi.org/10.1016/j.icarus.2018.03.010.

Gulkis, S., Allen, M., von Allmen, P., Beaudin, G., Biver, N., Bockelée-Morvan, D., Choukroun, M., Crovisier, J., Davidsson, B.J.R., Encrenaz, P., Encrenaz, T., Frerking,

M., Hartogh, P., Hofstadter, M., Ip, W.-H., Janssen, M., Jarchow, C., Keihm, S., Lee, S., Lellouch, E., Leyrat, C., Rezac, L., Schloerb, F.P., Spilker, T., 2015. Subsurface properties and early activity of comet 67P/Churyumov-Gerasimenko. Science 347, 709. https://doi.org/10.1126/science.aaa0709.

Gulkis, S., Frerking, M., Crovisier, J., Beaudin, G., Hartogh, P., Encrenaz, P., Koch, T., Kahn, C., Salinas, Y., Nowicki, R., Irigoyen, R., Janssen, M., Stek, P., Hofstadter, M., Allen, M., Backus, C., Kamp, L., Jarchow, C., Steinmetz, E., Deschamps, A., Krieg, J., Gheudin, M., Bockelée-Morvan, D., Biver, N., Encrenaz, T., Despois, D., Ip, W., Lellouch, E., Mann, I., Muhleman, D., Rauer, H., Schloerb, P., Spilker, T., 2007. MIRO: Microwave Instrument for Rosetta Orbiter. Space Sci. Rev. 128, 561–597. https://doi.org/10.1007/s11214-006-9032-y.

Hansen, K.C., Altwegg, K., Berthelier, J.J., Bieler, A., Biver, N., Bockelée-Morvan, D., Calmonte, U., Capaccioni, F., Combi, M.R., de Keyser, J., Fiethe, B., Fougere, N., Fuselier, S.A., Gasc, S., Gombosi, T.I., Huang, Z., Le Roy, L., Lee, S., Nilsson, H., Rubin, M., Shou, Y., Snodgrass, C., Tenishev, V., Toth, G., Tzou, C.Y., Wedlund, C.S., Rosina Team, 2016. Evolution of water production of 67P/Churyumov-Gerasimenko: an empirical model and a multi-instrument study. MNRAS 462, S491–S506. https://doi.org/10.1093/mnras/stw2413.

Hartogh, P., Hartmann, G.K., 1990. A high-resolution chirp transform spectrometer for microwave measurements. Meas. Sci. Technol. 1, 592–595. https://doi.org/10.1088/0957-0233/1/7/008.

Haser, L., 1957. Distribution d'intensité dans la tête d'une comète. Bull. Soc. R. Sci. Liege 43, 740–750.

Hässig, M., Altwegg, K., Balsiger, H., Bar-Nun, A., Berthelier, J.J., Bieler, A., Bochsler, P., Briois, C., Calmonte, U., Combi, M., De Keyser, J., Eberhardt, P., Fiethe, B., Fuselier, S.A., Galand, M., Gasc, S., Gombosi, T.I., Hansen, K.C., Jäckel, A., Keller, H.U., Kopp, E., Korth, A., Kührt, E., Le Roy, L., Mall, U., Marty, B., Mousis, O., Neefs, E., Owen, T., Rème, H., Rubin, M., Sémon, T., Tornow, C., Tzou, C.Y., Waite, J.H., Wurz, P., 2015. Time variability and heterogeneity in the coma of 67P/Churyumov-Gerasimenko. Science 347, 276. https://doi.org/10.1126/science.aaa0276.

Huebner, W.F., Benkhoff, J., Capria, M.-T., Coradini, A., De Sanctis, C., Orosei, R., Prialnik, D. (Eds.), 2006. Heat and Gas Diffusion in Comet Nuclei.

Jutzi, M., Benz, W., 2017. Formation of bi-lobed shapes by sub-catastrophic collisions. A late origin of comet 67P's structure. Astron. Astrophys. 597, A62. https://doi.org/10.1051/0004-6361/201628964.

Keller, H.U., Barbieri, C., Lamy, P., Rickman, H., Rodrigo, R., Wenzel, K.-P., Sierks, H., A'Hearn, M.F., Angrilli, F., Angulo, M., Bailey, M.E., Barthol, P., Barucci, M.A., Bertaux, J.-L., Bianchini, G., Boit, J.-L., Brown, V., Burns, J.A., Büttner, I., Castro, J.M., Cremonese, G., Curdt, W., da Deppo, V., Debei, S., de Cecco, M., Dohlen, K., Fornasier, S., Fulle, M., Germerott, D., Gliem, F., Guizzo, G.P., Hviid, S.F., Ip, W.H., Jorda, L., Koschny, D., Kramm, J.R., Kührt, E., Küppers, M., Lara, L.M., Llebaria, A., López, A., López-Jimenez, A., López-Moreno, J., Meller, R., Michalik, H., Michelena, M.D., Müller, R., Naletto, G., Origné, A., Parzianello, G., Pertile, M., Quintana, C., Ragazzoni, R., Ramous, P., Reiche, K.U., Reina, M., Rodríguez, J., Rousset, G., Sabau, L., Sanz, A., Sivan, J.P., Stöckner, K., Tabero, J., Telljohann, U., Thomas, N., Timon, V., Tomasch, G., Wittrock, T., Zaccariotto, M., 2007. OSIRIS the scientific camera system onboard Rosetta. Space Sci. Rev. 128, 433–506. https://doi.org/10.1007/s11214-006-9128-4.

Keller, H.U., Knollenberg, J., Markiewicz, W.J., 1994. Collimation of cometary dust jets and filaments. Planet. Space Sci. 42, 367–382. https://doi.org/10.1016/0032-0633(94)90126-0.

Lamy, P.L., Toth, I., Weaver, H.A., Jorda, L., Kaasalainen, M., Gutiérrez, P.J., 2006, Nov, Nov. Hubble space telescope observations of the nucleus and inner coma of comet 67P/Churyumov-Gerasimenko. Astron. Astrophys. 458, 669–678. https://doi.org/10.1051/0004-6361:20065253.

Le Roy, L., Altwegg, K., Balsiger, H., Berthelier, J.-J., Bieler, A., Briois, C., Calmonte, U., Combi, M.R., De Keyser, J., Dhooghe, F., Fiethe, B., Fuselier, S.A., Gasc, S., Gombosi, T.I., Hässig, M., Jäckel, A., Rubin, M., Tzou, C.-Y., 2015. Inventory of the volatiles on comet 67P/Churyumov-Gerasimenko from Rosetta/ROSINA. Astron. Astrophys. 583, A1. https://doi.org/10.1051/0004-6361/201526450.

Lee, S., von Allmen, P., Allen, M., Beaudin, G., Biver, N., Bockelée-Morvan, D., Choukroun, M., Crovisier, J., Encrenaz, P., Frerking, M., Gulkis, S., Hartogh, P., Hofstadter, M., Ip, W.-H., Janssen, M., Jarchow, C., Keihm, S., Lellouch, E., Leyrat, C., Rezac, L., Schloerb, F.P., Spilker, T., Gaskell, B., Jorda, L., Keller, H.U., Sierks, H., 2015. Spatial and diurnal variation of water outgassing on comet 67P/Churyumov-Gerasimenko observed from Rosetta/MIRO in August 2014. Astron. Astrophys. 583, A5. https://doi.org/10.1051/0004-6361/201526155.

Liao, Y., 2017. submitted. Ph.D. thesis. Universitt Bern, Switzerland.

Liao, Y., Marschall, R., Su, C.C., Wu, J.S., Lai, I.L., Pinzon, O., Thomas, N., 2018. Water vapor deposition from the inner gas coma onto the nucleus of Comet 67P/Churyumov-Gerasimenko. Planet. Space Sci. 157, 1–9. https://doi.org/10.1016/j.pss.2018.04.014.

Liao, Y., Su, C., Marschall, R., Thomas, N., 2015. Earth Plan. Sci. Lett submitted.

Lin, Z.Y., Lai, I.L., Su, C.C., Ip, W.H., Lee, J.C., Wu, J.S., Vincent, J.B., La Forgia, F., Sierks, H., Barbieri, C., Lamy, P.L., Rodrigo, R., Koschny, D., Rickman, H., Keller, H.U., Agarwal, J., A'Hearn, M.F., Barucci, M.A., Bertaux, J.L., Bertini, I., Bodewits, D., Cremonese, G., Da Deppo, V., Davidsson, B., Debei, S., De Cecco, M., Fornasier, S., Fulle, M., Groussin, O., Gutiérrez, P.J., Güttler, C., Hviid, S.F., Jorda, L., Knollenberg, J., Kovacs, G., Kramm, J.R., Kührt, E., Küppers, M., Lara, L.M., Lazzarin, M., López-Moreno, J.J., Lowry, S., Marzari, F., Michalik, H., Mottola, S., Naletto, G., Oklay, N., Pajola, M., Rożek, A., Thomas, N., Tubiana, C., 2016. Observations and analysis of a curved jet in the coma of comet 67P /Churyumov-Gerasimenko. Astron. Astrophys. 588, L3. https://doi.org/10.1051/0004-6361/201527784.

Marboeuf, U., Schmitt, B., Petit, J.M., Mousis, O., Fray, N., 2012. A cometary nucleus model taking into account all phase changes of water ice: amorphous, crystalline, and clathrate. Astron. Astrophys. 542, A82. https://doi.org/10.1051/0004-6361/201118176.

Marschall, R., Mottola, S., Su, C.C., Liao, Y., Rubin, M., Wu, J.S., Thomas, N., Altwegg, K., Sierks, H., Ip, W.H., Keller, H.U., Knollenberg, J., Kührt, E., Lai, I.L., Skorov, Y., Jorda, L., Preusker, F., Scholten, F., Vincent, J.B., Osiris Team, Rosina Team, 2017. Cliffs versus plains: can ROSINA/COPS and OSIRIS data of comet 67P /Churyumov-Gerasimenko in autumn 2014 constrain inhomogeneous outgassing? Astron. Astrophys. 605, A112. https://doi.org/10.1051/0004-6361/201730849.

Marschall, R., Su, C.C., Liao, Y., Thomas, N., Altwegg, K., Sierks, H., Ip, W.-H., Keller, H.U., Knollenberg, J., Kührt, E., Lai, I.L., Rubin, M., Skorov, Y., Wu, J.S., Jorda, L., Preusker, F., Scholten, F., Gracia-Berná, A., Gicquel, A., Naletto, G., Shi, X., Vincent, J.-B., 2016. Modelling observations of the inner gas and dust coma of comet 67P/Churyumov-Gerasimenko using ROSINA/COPS and OSIRIS data: first results. Astron. Astrophys. 589, A90. https://doi.org/10.1051/0004-6361/201628085.

Marshall, D., Groussin, O., Vincent, J.-B., Brouet, Y., Kappel, D., Arnold, G., Capria, M., Filacchione, G., Hartogh, P., Hofstadter, Ip, W.-H., Jorda, L., Kuehrt, E., Lellouch, E., Mottola, S., Rezac, L., Rodrigo, R., Rodionov, S., Schloerb, P., Thomas, N., 2018. Thermal inertia and roughness of the nucleus of comet 67p/Churyumov-Gerasimenko from miro and virtis observations. Astron. Astrophys.

Marshall, D.W., Hartogh, P., Rezac, L., von Allmen, P., Biver, N., Bockelée-Morvan, D., Crovisier, J., Encrenaz, P., Gulkis, S., Hofstadter, M., Ip, W.H., Jarchow, C., Lee, S., Lellouch, E., 2017. Spatially resolved evolution of the local H2O production rates of comet 67P/Churyumov-Gerasimenko from the MIRO instrument on Rosetta. Astron. Astrophys. 603, A87. https://doi.org/10.1051/0004-6361/201730502.

Menke, W., 1989. Geophysical Data Analysis: Discrete Inverse Theory.

Merouane, S., Zaprudin, B., Stenzel, O., Langevin, Y., Altobelli, N., Della Corte, V., Fischer, H., Fulle, M., Hornung, K., Silén, J., Ligier, N., Rotundi, A., Ryno, J., Schulz, R., Hilchenbach, M., Kissel, J., Cosima Team, 2016. Dust particle flux and size distribution in the coma of 67P/Churyumov-Gerasimenko measured in situ by the COSIMA instrument on board Rosetta. Astron. Astrophys. 596, A87. https://doi.org/10.1051/0004-6361/201527958.

Migliorini, A., Piccioni, G., Capaccioni, F., Filacchione, G., Bockelée-Morvan, D., Erard, S., Leyrat, C., Combi, M.R., Fougere, N., Crovisier, J., Taylor, F.W., De Sanctis, M.C., Capria, M.T., Grassi, D., Rinaldi, G., Tozzi, G.P., Fink, U., 2016. Water and carbon dioxide distribution in the 67P/Churyumov-Gerasimenko coma from VIRTIS-M infrared observations. Astron. Astrophys. 589, A45. https://doi.org/10.1051/0004-6361/201527661.

Preusker, F., Scholten, F., Matz, K.D., Roatsch, T., Hviid, S.F., Mottola, S., Knollenberg, J., Kührt, E., Pajola, M., Oklay, N., Vincent, J.B., Davidsson, B., A'Hearn, M.F., Agarwal, J., Barbieri, C., Barucci, M.A., Bertaux, J.L., Bertini, I., Cremonese, G., Da Deppo, V., Debei, S., De Cecco, M., Fornasier, S., Fulle, M., Groussin, O., Gutiérrez, P.J., Güttler, C., Ip, W.H., Jorda, L., Keller, H.U., Koschny, D., Kramm, J.R., Küppers, M., Lamy, P., Lara, L.M., Lazzarin, M., Lopez Moreno, J.J., Marzari, F., Massironi, M., Naletto, G., Rickman, H., Rodrigo, R., Sierks, H., Thomas, N., Tubiana, C., 2017. The global meter-level shape model of comet 67P/Churyumov-Gerasimenko. Astron. Astrophys. 607, L1. https://doi.org/10.1051/0004-6361/201731798.

Raponi, A., Ciarniello, M., Capaccioni, F., Filacchione, G., Tosi, F., De Sanctis, M.C., Capria, M.T., Barucci, M.A., Longobardo, A., Palomba, E., Kappel, D., Arnold, G., Mottola, S., Rousseau, B., Quirico, E., Rinaldi, G., Erard, S., Bockelee-Morvan, D., Leyrat, C., 2016. The temporal evolution of exposed water ice-rich areas on the surface of 67P/Churyumov-Gerasimenko: spectral analysis. MNRAS 462, S476–S490. https://doi.org/10.1093/mnras/stw3281.

Rodgers, C.D., 1976, Nov, Nov. Retrieval of atmospheric temperature and composition from remote measurements of thermal radiation. Rev. Geophys. Space Phys. 14, 609. https://doi.org/10.1029/RG014i004p00609.

Rodgers, C.D., 2000. Inverse Methods for Atmospheric Sounding: Theory and Practice. World Scientific Publishing Cohttps://doi.org/10.1142/3171.

Schloerb, F.P., Keihm, S., von Allmen, P., Choukroun, M., Lellouch, E., Leyrat, C., Beaudin, G., Biver, N., Bockelée-Morvan, D., Crovisier, J., Encrenaz, P., Gaskell, R., Gulkis, S., Hartogh, P., Hofstadter, M., Ip, W.-H., Janssen, M., Jarchow, C., Jorda, L., Keller, H.U., Lee, S., Rezac, L., Sierks, H., 2015. MIRO observations of subsurface temperatures of the nucleus of 67P/Churyumov-Gerasimenko. Astron. Astrophys. 583, A29. https://doi.org/10.1051/0004-6361/201526152.

Shou, Y., Combi, M., Toth, G., Tenishev, V., Fougere, N., Jia, X., Rubin, M., Huang, Z., Hansen, K., Gombosi, T., 2017. A new 3D multi-fluid dust model: a study of the effects of activity and nucleus rotation on dust grain behavior at comet 67P/Churyumov- Gerasimenko. ApJ 850, 72. https://doi.org/10.3847/1538-4357/aa91ca.

Sierks, H., Barbieri, C., Lamy, P.L., Rodrigo, R., Koschny, D., Rickman, H., Keller, H.U., Agarwal, J., A'Hearn, M.F., Angrilli, F., Auger, A.-T., Barucci, M.A., Bertaux, J.-L., Bertini, I., Besse, S., Bodewits, D., Capanna, C., Cremonese, G., Da Deppo, V., Davidsson, B., Debei, S., De Cecco, M., Ferri, F., Fornasier, S., Fulle, M., Gaskell, R., Giacomini, L., Groussin, O., Gutierrez-Marques, P., Gutiérrez, P.J., Güttler, C., Hoekzema, N., Hviid, S.F., Ip, W.H., Jorda, L., Knollenberg, J., Kovacs, G., Kramm, J.R., Kührt, E., Küppers, M., La Forgia, F., Lara, L.M., Lazzarin, M., Leyrat, C., Lopez Moreno, J.J., Magrin, S., Marchi, S., Marzari, F., Massironi, M., Michalik, H., Moissl, R., Mottola, S., Naletto, G., Oklay, N., Pajola, M., Pertile, M., Preusker, F., Sabau, L., Scholten, F., Snodgrass, C., Thomas, N., Tubiana, C., Vincent, J.B., Wenzel, K.P., Zaccariotto, M., Pätzold, M., 2015. On the nucleus structure and activity of comet 67P/Churyumov-Gerasimenko. Science 347, 1044. https://doi.org/10.1126/science.aaa1044.

Su, C.C., 2013. Ph.D. thesis. National Chiao Tung Univ., Taiwan.

Tenishev, V., Fougere, N., Borovikov, D., Combi, M.R., Bieler, A., Hansen, K.C., Gombosi, T.I., Migliorini, A., Capaccioni, F., Rinaldi, G., Filacchione, G., Kolokolova, L., Fink, U., 2016. Analysis of the dust jet imaged by Rosetta VIRTIS-M in the coma of comet 67P/Churyumov-Gerasimenko on 2015 April 12. MNRAS 462, S370–S375. https://doi.org/10.1093/mnras/stw2793.

Thomas, N., Maarry, M.E., Theologou, P., Preusker, F., Scholten, F., Jorda, L., Hviid, S., Marschall, R., Kührt, E., Naletto, G., Sierks, H., Lamy, P., Rodrigo, R., Koschny, D., Davidsson, B., Barucci, M., Bertaux, J., Bertini, I., Bodewits, D., Cremonese, G., Deppo, V.D., Debei, S., Cecco, M.D., Fornasier, S., Fulle, M., Groussin, O., Gutiérrez, P., Güttler, C., Ip, W., Keller, H., Knollenberg, J., Lara, L., Lazzarin, M., Lpez-Moreno, J., Marzari, F., Tubiana, C., Vincent, J., 2018. Regional unit definition for the nucleus of comet 67p/churyumov-Gerasimenko on the shap7 model. Planet. Space Sci. https://doi.org/10.1016/j.pss.2018.05.019. http://www.sciencedirect.com/science/article/pii/S0032063318300692.

Tubiana, C., Güttler, C., Kovacs, G., Bertini, I., Bodewits, D., Fornasier, S., Lara, L., La Forgia, F., Magrin, S., Pajola, M., Sierks, H., Barbieri, C., Lamy, P.L., Rodrigo, R., Koschny, D., Rickman, H., Keller, H.U., Agarwal, J., A'Hearn, M.F., Barucci, M.A., Bertaux, J.L., Besse, S., Boudreault, S., Cremonese, G., Da Deppo, V., Davidsson, B., Debei, S., De Cecco, M., El-Maarry, M.R., Fulle, M., Groussin, O., Gutiérrez-Marques, P., Gutiérrez, P.J., Hoekzema, N., Hofmann, M., Hviid, S.F., Ip, W.H., Jorda, L., Knollenberg, J., Kramm, J.R., Kührt, E., Küppers, M., Lazzarin, M., Lopez Moreno, J.J., Marzari, F., Massironi, M., Michalik, H., Moissl, R., Naletto, G., Oklay, N., Scholten, F., Shi, X., Thomas, N., Vincent, J.B., 2015. Scientific assessment of the quality of OSIRIS images. Astron. Astrophys. 583, A46. https://doi.org/10.1051/0004-6361/201525985.

Wu, J.-S., Lian, Y., 2003. Parallel three-dimensional direct simulation Monte Carlo method and its applications. Comput. Fluids 32, 1133–1160.

Wu, J.-S., Tseng, K.-C., 2005. Parallel DSMC method using dynamic domain decomposition. Int. J. Numer. Methods Eng. 63, 37–76. https://doi.org/10.1002/nme.1232.

Wu, J.-S., Tseng, K.-C., Wu, F.-Y., 2004. Parallel three-dimensional DSMC method using mesh refinement and variable time-step scheme. Comput. Phys. Commun. 162, 166–187. https://doi.org/10.1016/j.cpc.2004.07.004.

Zakharov, V.V., Ivanovski, S.L., Crifo, J.F., Della Corte, V., Rotundi, A., Fulle, M., 2018. Asymptotics for spherical particle motion in a spherically expanding flow. Icarus 312, 121–127. https://doi.org/10.1016/j.icarus.2018.04.030.